

Measurements of the UV background at $4.6 < z < 6.4$ using the quasar proximity effect ^{*}

Alexander P. Calverley¹ †, George D. Becker¹, Martin G. Haehnelt¹ and James S. Bolton²

¹*Kavli Institute for Cosmology and Institute of Astronomy, Madingley Road, Cambridge, CB3 0HA*

²*School of Physics, University of Melbourne, Parkville, VIC 3010, Australia*

Accepted 2010 November 23. Received 2010 November 08; in original form 2010 September 13

ABSTRACT

We present measurements of the ionising ultraviolet background (UVB) at $z \sim 5-6$ using the quasar proximity effect. The fifteen quasars in our sample cover the range $4.6 < z_q < 6.4$, enabling the first proximity effect measurements of the UVB at $z > 5$. The metagalactic hydrogen ionisation rate, Γ_{bkg} , was determined by modelling the combined ionisation field from the quasar and the UVB in the proximity zone on a pixel-by-pixel basis. The optical depths in the spectra were corrected for the expected effect of the quasar until the mean flux in the proximity region equalled that in the average Ly α forest, and from this we make a measurement of Γ_{bkg} . A number of systematic effects were tested using synthetic spectra. Noise in the flux was found to be the largest source of bias at $z \sim 5$, while uncertainties in the mean transmitted Ly α flux are responsible for the largest bias at $z \sim 6$. The impacts of large-scale overdensities and Lyman limit systems on Γ_{bkg} were also investigated, but found to be small at $z > 5$. We find a decline in Γ_{bkg} with redshift, from $\log(\Gamma_{\text{bkg}}) = -12.15 \pm 0.16$ at $z \sim 5$ to $\log(\Gamma_{\text{bkg}}) = -12.84 \pm 0.18$ at $z \sim 6$ (1σ errors). Compared to UVB measurements at lower redshifts, our measurements suggest a drop of a factor of five in the H I photoionisation rate between $z \sim 4$ and $z \sim 6$. The decline of Γ_{bkg} appears to be gradual, and we find no evidence for a sudden change in the UVB at any redshift that would indicate a rapid change in the attenuation length of ionising photons. Combined with recent measurements of the evolution of the mean free path of ionising photons, our results imply decline in the emissivity of ionising photons by roughly a factor of two from $z \sim 5$ to 6, albeit with significant uncertainty due to the measurement errors in both Γ_{bkg} and the mean free path.

Key words: intergalactic medium - quasars: absorption lines - cosmology: observations - cosmology: early Universe

1 INTRODUCTION

The metagalactic ultraviolet background (UVB) is the net radiation field responsible for keeping the Universe ionised from the end of reionization to the present day. The relative contributions from galaxies and quasars, as well as filtering by the intergalactic medium (IGM) itself, determine the intensity and spectrum

of the UVB (e.g. Bechtold et al. 1987; Haardt & Madau 1996; Fardal et al. 1998; Haardt & Madau 2001). Thus by measuring the UVB one can hope to place constraints on the evolution of the source population with redshift.

Of particular interest is the evolution of the UVB at $z \sim 6$. The appearance of Gunn-Peterson (GP) troughs in the spectra of the highest-redshift known quasars has been interpreted as evidence for a sharp downturn in the UVB at $z > 6$ signalling the end of reionization (e.g., Fan et al. 2006b). However, the diminishing transmitted flux is also consistent with a more slowly-evolving UVB and IGM density field (Bolton & Haehnelt 2007b; Becker et al. 2007).

The bulk of the ionising photons at $z > 6$ that make up the UVB are believed to come from low-luminosity galaxies (Richard et al. 2006; Stark et al. 2007; Richard et al. 2008;

^{*} A part of the observations were made at the W.M. Keck Observatory which is operated as a scientific partnership between the California Institute of Technology and the University of California; it was made possible by the generous support of the W.M. Keck Foundation. This paper also includes data gathered with the 6.5 meter Magellan Telescopes located at Las Campanas Observatory, Chile.

† E-mail: acalver@ast.cam.ac.uk

Srbnovsky & Wyithe 2010; Oesch et al. 2010). Direct searches for these sources at $z \gtrsim 6 - 10$ have taken advantage of recent very deep optical and near-infrared imaging from both the ground and space (Bunker et al. 2004; Bouwens et al. 2006; Yoshida et al. 2006; Bouwens et al. 2008; Ouchi et al. 2009). The majority of these faint galaxies, however, still remain below current detection thresholds (e.g. Bouwens et al. 2010).

The quasar proximity effect has been a classic tool for directly measuring the intensity of the UVB at high redshifts. Since quasars are highly luminous, their output of ionising photons will dominate over that of the UVB out to large (up to several proper Mpc) distances. This produces a region of enhanced transmission near the redshift of the quasar, first noted by Carswell et al. (1982), known as the ‘proximity region.’ The size of this region depends both on the quasar luminosity and the intensity of the UVB. For a known quasar luminosity, therefore, the UVB can be estimated by measuring the extent of the proximity zone. Classically, the proximity effect has been measured by comparing column densities of the H I Ly α absorption lines in the forest with those close to the quasar (Murdoch et al. 1986; Tytler 1987; Carswell et al. 1987; Scott et al. 2000; Bajtlik et al. 1988, hereafter BDO), although a variety of flux statistics have also been used (Liske & Williger 2001; Dall’Aglio et al. 2008; Dall’Aglio & Gnedin 2010). Altogether, proximity effect studies have delivered measurements of the UVB from $z \sim 0.5$ (Kulkarni & Fall 1993) to $z \sim 4.5$ (Dall’Aglio et al. 2009).

More recently, an alternative method of estimating the UVB has been developed which uses the mean flux in the Ly α forest in combination with numerical simulations. The UVB in the simulation is adjusted until the mean flux in artificial Ly α forest spectra is equal to that in the real data (see e.g., Rauch et al. 1997; Songaila et al. 1999; Tytler et al. 2004; Bolton et al. 2005; Kirkman et al. 2005; Jena et al. 2005). At $z > 4.5$, the UVB has so far only been determined using this method (McDonald & Miralda-Escudé 2001; Meiksin & White 2004; Bolton & Haehnelt 2007b; Wyithe & Bolton 2010). At $z \sim 5 - 6$, however, converting the mean flux into an ionisation rate depends sensitively on modelling the gas density distribution at very low densities (e.g. Miralda-Escudé et al. 2000). Not only is this a challenge numerically (Bolton & Becker 2009), but the optical depth distribution will depend on the properties of the simulation, including the gas temperature.

At $z < 4.5$, estimates of the UVB from the proximity effect and flux decrement methods can be directly compared. These are generally discrepant at $2 < z < 4$, with the proximity effect estimates systematically higher for most studies. Recent proximity effect papers suggest that there is a competition between the effect of the enhanced intensity of the UVB and the overdensity of matter close to the quasar. Classically, the proximity effect assumes that the density distribution close to the quasar is the same as that in the general IGM. Not accounting for overdensities may therefore cause the UVB to be overestimated by up to a factor of 3 (Loeb & Eisenstein 1995). By using an independent measure of the UVB from flux decrements, Rollinde et al. (2005) found tentative evidence that quasars at $z = 2 - 3$ may reside in haloes as massive as $\sim 10^{14} M_{\odot}$, similar to the most massive halo in the Millennium simulation. Guimarães et al. (2007) have claimed to detect a similar effect at $z \sim 4$. Other recent papers, however, have claimed to have overcome the environmental bias of an enhanced average density in the proximity zone. Dall’Aglio et al. (2008) report that with their measurement method only 10 per cent of their sample at $2 \lesssim z \lesssim 4.5$ showed significant excess absorption attributable to

an overdense environment, and that for the majority of the quasars in their sample their proximity effect measurement of the UVB did not appear to be affected by an overdense quasar environment (at least on scales > 3 Mpc).

In this paper, rather than identify individual lines, which becomes increasingly difficult at $z > 4$, we further develop a variant on the ‘flux-transmission’ method (Liske & Williger 2001) to measure the UVB intensity at $z > 4.5$. At lower redshifts this has been used to compare the mean flux averaged over extended sections of the spectrum near the quasar redshift to the mean flux in the forest. Rather than compute the mean flux in sections, we consider individual pixel optical depths across the proximity region. The optical depths are modified to remove the presumed effect of the quasar, until the proximity region has the same mean flux as the forest at that redshift. The characteristic scale length of the quasar model is then combined with the quasar luminosity to estimate the UVB. This simple approach avoids a direct dependence on simulations as it does not require the optical depth distribution of the forest to be known *a priori*. We use, however, simulations extensively to estimate the bias and uncertainties of our method.

The remainder of this paper is organised as follows: In section 2 we describe the observational data as well as the hydrodynamical simulations used. In section 3 we detail the proximity effect analysis, and the sources of systematic bias such as the effect of the quasar environment. The results are presented and their implications discussed in Section 4. Finally, we present our conclusions in Section 5. Throughout this paper we assume a flat Universe and cosmological parameters taken from the mean of the WMAP 5 year data set (Komatsu et al. 2009), with Hubble constant $H_0 = 72 \text{ km s}^{-1} \text{ Mpc}^{-1}$ and density parameters $(\Omega_m, \Omega_{\Lambda}) = (0.26, 0.74)$.

2 DATA AND MODELS

2.1 Observed spectra

The quasar spectra used in this paper were taken with either the Keck or Magellan telescopes. The majority of the quasars at $z > 5$ were observed with the High Resolution Echelle Spectrometer (HIRES; Vogt et al. 1994) on the 10 m Keck I telescope, and reduced using a custom set of IDL routines and optimal sky subtraction techniques as detailed in Becker et al. (2006, 2007). All of these observations were made with the 0.86" slit with $R = 40\,000$, and so the velocity resolution is 6.7 km s^{-1} .

The majority of the quasars at $z < 5$ were observed using the 6.5 m Magellan-II Clay and the Magellan Inamori Kyocera Echelle (MIKE) spectrograph (Bernstein et al. 2003) and reduced with a similar custom pipeline. The velocity resolution is roughly half that of the HIRES spectra at 13.6 km s^{-1} . A list of the targets is shown in Table 1.

Quasar redshifts were taken either from the CO and Mg II redshifts presented in Carilli et al. (2010), or from the spectra themselves by identifying the redshift at which the Ly α forest appears to start. Errors on the redshifts measured from the apparent start of the Ly α forest were estimated by comparing to more precise redshifts from Mg II and CO where available, or those in the SDSS. All the objects have photometry in the SDSS, and those at $z < 5.5$ also have flux-calibrated spectra in the SDSS archive. Continuum magnitudes for those at $z > 5.5$ were taken from the discovery papers (Fan et al. 2001, 2003, 2004, 2006b), whilst fluxes for those at $z < 5.5$ were measured from the SDSS spectra. In both cases the

Table 1. The list of quasars included in this paper. Columns give the quasar name and redshift, details of the observations, and the average signal-to-noise per pixel in the $40h^{-1}$ comoving Mpc closest to the quasar redshift, after masking out skyline residuals (see Section 3.3).

Name	z_q	Inst.	Dates	t_{exp} (hrs)	Ref.	S/N
SDSS J1148+5251	6.42	HIRES	Jan 2005 - Feb 2005	14.2 ^a	1	16
SDSS J1030+0524	6.31	HIRES	Feb 2005	10.0	1	12
SDSS J1623+3112	6.25	HIRES	Jun 2005	12.5	1	11
SDSS J0818+1722	6.02	HIRES	Feb 2006	8.3	2	12
SDSS J1306+0356	6.02	MIKE	Feb 2007	6.7	4	14
SDSS J0002+2550	5.82	HIRES	Jan 2005 - Jul 2008	14.2	1,4	21
SDSS J0836+0054	5.81	HIRES	Jan 2005	12.5 ^a	1	19
SDSS J0231-0728	5.41	HIRES	Jan 2005 - Feb 2005	10.0	1	14
SDSS J1659+2709	5.33	HIRES	Sep 2007 - Jul 2008	11.7	3	32
SDSS J0915+4924	5.20	HIRES	Feb 2005	10.0	1	23
SDSS J1204-0021	5.09	HIRES	Jan 2005 - Feb 2005	6.7	1	17
SDSS J0011+1440	4.97	HIRES	Sep 2007	6.7	3	47
SDSS J2225-0014	4.89	MIKE	Oct 2007	5.0	4	23
SDSS J1616+0501	4.88	MIKE	Mar 2008	3.3	4	21
SDSS J2147-0838	4.59	MIKE	Oct 2007	8.3	3	51

^a The present reductions include only data taken with the upgraded detector.

References:

1 - Becker et al. (2006); 2 - Becker et al. (2007); 3 - Becker et al. (2010); 4 - This paper

Table 2. Mass resolution and box size (comoving) of the hydrodynamical simulations used in this work. Model C was primarily used to simulate quasar proximity zones.

Model	L [Mpc/h]	Total particle number	M_{gas} [M_{\odot}/h]
A	20	2×100^3	1.03×10^8
B	20	2×200^3	1.29×10^7
C	20	2×400^3	1.61×10^6
D	40	2×200^3	1.03×10^8
E	40	2×400^3	1.29×10^7
F	80	2×400^3	1.03×10^8

continuum flux was measured at a rest wavelength of 1280 Å. The error in the flux measured from the SDSS spectra is conservatively taken to be 0.5×10^{-17} erg cm⁻² s⁻¹ Å⁻¹.

All the spectra were normalised following the method described in Bolton et al. (2010). The spectrum is first divided through by a power-law $F_{\nu} \propto \nu^{-0.5}$, normalised at 1280 $(1+z)$ Å, and the Ly α emission line is then fitted with a slowly varying spline. It is difficult to fit the continuum over the forest at these redshifts due to the low flux levels, however in the proximity region the transmitted flux maxima will be nearer to the continuum, and so is estimated to be within ~ 20 per cent of the correct value over the region of interest.

2.2 Simulated spectra

Simulations of the IGM at high redshift were used to test the method and to explore potential sources of systematic error. The simulations are the same as those in Bolton & Becker (2009) and were performed using a customised version of the parallel Tree-SPH code GADGET-3, an updated version of the publicly available code GADGET-2 (Springel 2005). The simulations assume the cosmological parameters $(h, \Omega_m, \Omega_{\Lambda}, \Omega_b h^2, \sigma_8) = (0.72, 0.26, 0.74, 0.024, 0.85)$, have both dark matter and gas components, and were started at $z = 99$ with initial conditions gen-

erated with the transfer function of Eisenstein & Hu (1999). Each simulation uses the UVB model of Haardt & Madau (2001) with contributions from both galaxies and quasars, and is switched on at $z = 9$ and applied in the optically thin limit. Our fiducial run is a $20h^{-1}$ (comoving) Mpc box with 2×400^3 particles (Model C). Simulations with other box sizes and particle numbers were used to test the dependence of the environmental bias due to an enhanced average density on the mass of the host halo, and are summarised in Table 2.

Simulated Ly α spectra were constructed from line-of-sight density, peculiar velocity, neutral H I fraction and temperature fields. For the main analysis this was done for 1024 random sightlines drawn parallel to the box boundaries (e.g. Theuns et al. 1998), with outputs at $z = (2, 3, 4, 5, 6)$. Each sightline is 1024 pixels long. Proximity zones were introduced into the spectra by modifying the neutral H I fraction (in real space) with the ionising intensity falling off as $1/r^2$, before convolving with the other fields to derive the optical depth (in velocity space). The spectra were convolved with a Gaussian with FWHM equal to the velocity resolution of the instrument that was being modelled (6.7 km s^{-1} for HIRES and 13.6 km s^{-1} for MIKE), before being resampled at the instrument pixel resolution (2.1 km s^{-1} and 5.0 km s^{-1} respectively). Gaussian distributed noise, as well as other imperfections, could then be added. Additionally, sightlines were drawn through the most massive haloes for the analysis described in Section 3.4.2. The haloes were identified using a friends-of-friends algorithm with a linking length of 0.2. For the analysis in the rest of this paper sightlines of $40h^{-1}$ comoving Mpc were used. For Models A-C several random sightlines were combined for this.

3 ANALYSIS

3.1 Proximity effect formalism

As mentioned in Section 1, the ionising flux from a quasar will locally dominate over the UVB in setting the ionisation state of the IGM. This leads to increased transmission near to the quasar compared to the transmission in the forest (the ‘proximity effect’).

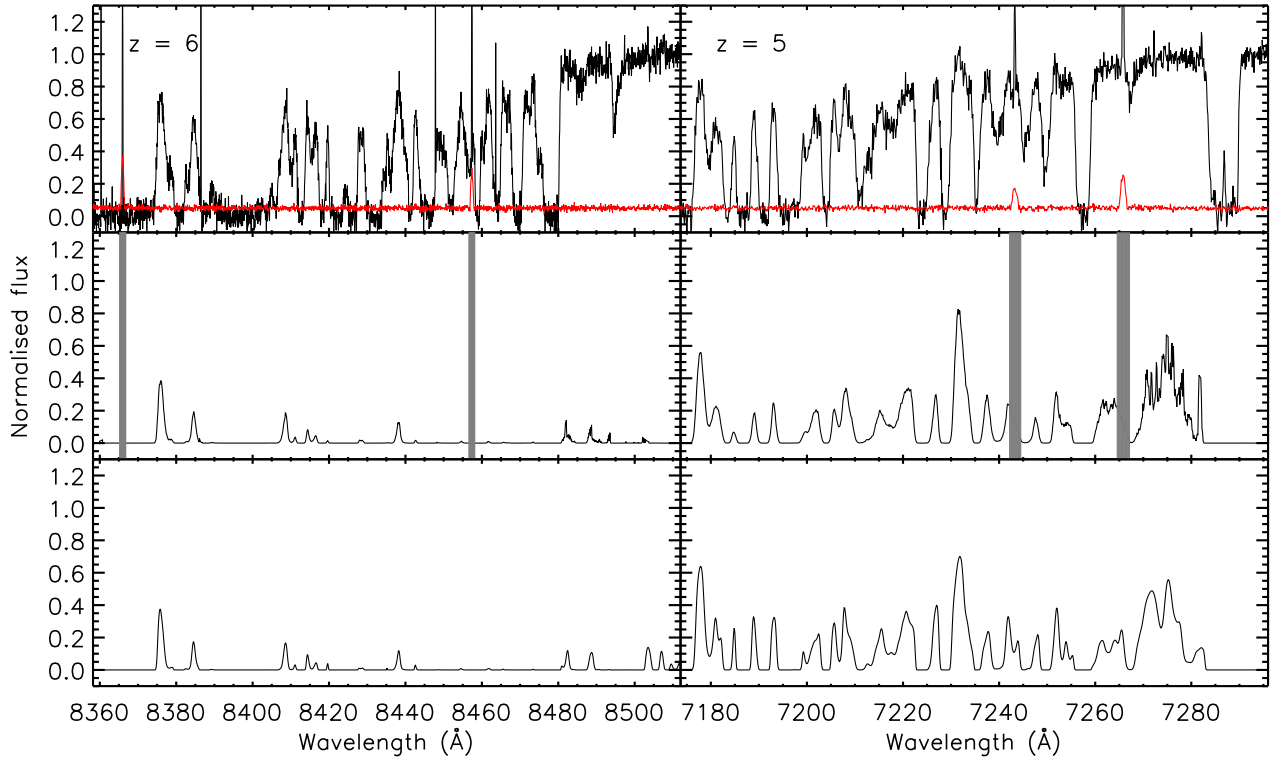


Figure 1. *Top panels:* Simulated sightlines at $z = 6$ (left) and $z = 5$ (right). Each sightline is $40h^{-1}$ comoving Mpc long, with $R_{\text{eq}} = 10$ proper Mpc and $S/N = 20$. The resolution for the $z = 6$ spectrum is equal to that of HIRES, whilst the spectrum at $z = 5$ has resolution equal to that of MIKE. The red line is the simulated error array. Artifacts such as bad pixels and skyline residuals have also been introduced. $\text{Ly}\alpha$ at the redshift of the quasar is on the far right of each panel. *Middle panels:* The spectra smoothed according to their noise properties (see Section 3.3), and with optical depths altered such that $\Delta F = 0$ (see Equation 10). The grey regions mark parts of the spectra that were masked out automatically (primarily skyline residuals). *Bottom panels:* The original $\text{Ly}\alpha$ forest for these sightlines. The similarity between these spectra and those in the middle panels provides a good check that the method is working correctly.

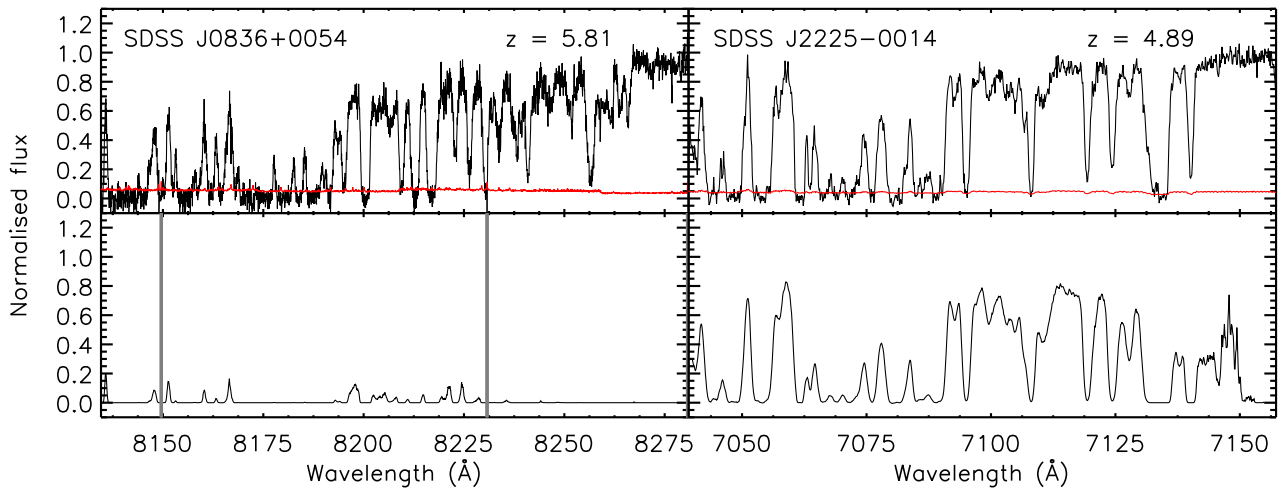


Figure 2. Same as Fig. 1, but for a small sample of the observed spectra. *Top panels:* The normalised spectrum of SDSS J0836+0054 at $z = 5.810$ taken with the HIRES instrument (left), and the normalised spectrum of SDSS J2225-0014 at $z = 4.886$ taken with MIKE (right). The length of each spectrum corresponds to $40h^{-1}$ comoving Mpc, and the red line is the observed error array. $\text{Ly}\alpha$ at the redshift of the quasar is on the far right of each panel. *Bottom panels:* The smoothed spectra with optical depths modified assuming an R_{eq} of the size quoted in Table 5. The grey regions mark parts of the spectra that were masked out automatically.

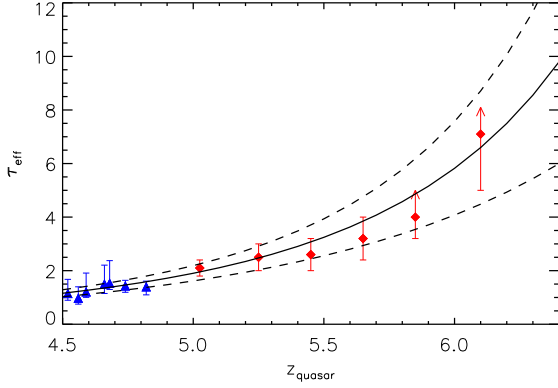


Figure 3. Our adopted fit to the evolution of τ_{eff} with redshift. The blue triangles are from measures of the flux in the forest from Songaila (2004), whilst the red diamonds are the binned values from Fan et al. (2006a). The solid line gives the Becker et al. (2007) relation for the evolution of τ_{eff} with redshift, which we adopt for this study. The 1σ error in τ_{eff} is marked with the dashed lines and was taken to be 10 per cent at $z = 4$, 15 per cent at $z = 5$ and 30 per cent at $z = 6$, with the error at other redshifts calculated by quadratic extrapolation.

BDO first translated this increased transmission (through a reduction in the number of strong absorption troughs) into a measure of the photoionisation rate of hydrogen caused by the UVB, Γ_{bkg} . More recently, measurements have been made of the proximity effect using flux transmission statistics rather than line-counting as done by BDO. The average transmission measured close to the quasar is thereby compared to that of the average Ly α forest (e.g. Liske & Williger 2001).

The optical depth, τ , is related to the normalised flux, $F = e^{-\tau}$. In the simplest model where the quasar lies in a typical region of the IGM, and neglecting all motion of the gas and any temperature gradients that may exist as one approaches the quasar, the optical depth at any point can be described as

$$\tau = \tau_{\text{forest}} [1 + \omega(r)]^{-1}, \quad (1)$$

where τ_{forest} is the optical depth that would be measured in the absence of the quasar (i.e. the typical value for the forest at that redshift), and

$$\omega(r) = \frac{\Gamma_{\text{q}}(r)}{\Gamma_{\text{bkg}}}. \quad (2)$$

Here, $\Gamma_{\text{q}}(r)$ is the H I photoionisation rate of the quasar at proper distance r , and Γ_{bkg} is the H I photoionisation rate of the UVB, assumed to be spatially uniform for a given redshift. The distance from the quasar, r , is approximately

$$r \simeq \frac{c}{H(z)} \frac{\Delta z}{1+z}. \quad (3)$$

We further define a characteristic length R_{eq} to be the distance from the quasar where the photoionisation rate from the UVB equals that from the quasar, i.e. $\Gamma_{\text{q}}(R_{\text{eq}}) = \Gamma_{\text{bkg}}$. With this definition, Equation 1 can then be rewritten as

$$\tau = \tau_{\text{forest}} \left[1 + \left(\frac{r}{R_{\text{eq}}} \right)^{-2} \right]^{-1}. \quad (4)$$

It must be emphasised that R_{eq} is different to proximity region sizes as defined in the literature. At high redshift the proximity region ‘size’ is typically defined to be the maximum extent of the

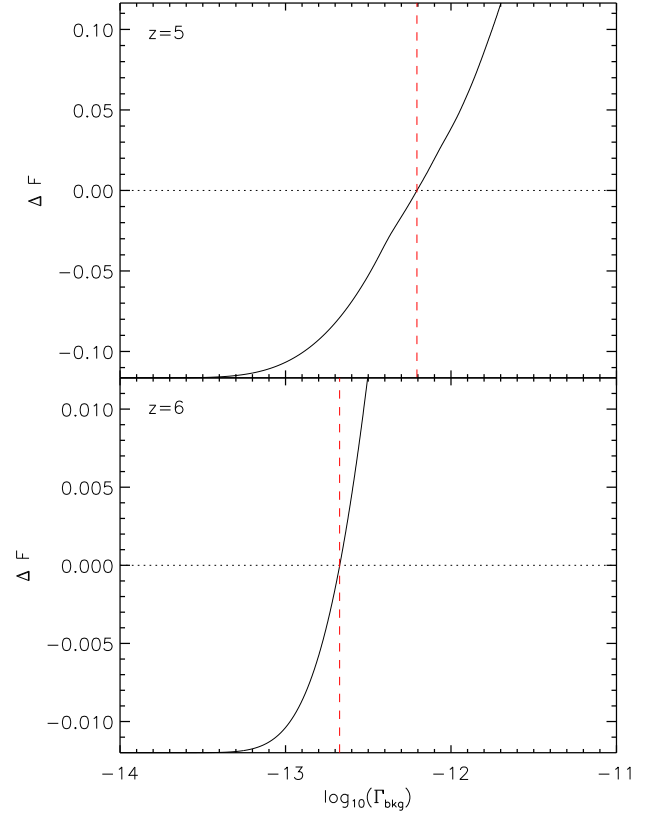


Figure 4. *Top panel:* The variation of ΔF with $\log(\Gamma_{\text{bkg}})$ of a simulated quasar spectrum at $z = 5$. The dotted line marks $\Delta F = 0$ and the dashed red line shows the estimated value of $\log(\Gamma_{\text{bkg}})$. For this particular input spectrum $\Delta F = 0$ at $\log(\Gamma_{\text{bkg}}) = -12.206$. The curve asymptotes as the mean flux becomes zero. *Bottom panel:* Same as the top but for a simulated quasar at $z = 6$. The curve is steeper, and so if the mean flux has been overestimated by some factor, this will result in a smaller change in the estimated $\log(\Gamma_{\text{bkg}})$ at $z = 6$ than at $z = 5$.

enhanced transmitted flux (e.g. the first point at which the transmission drops to 0.1 in the spectrum when smoothed with a 20 \AA filter, Fan et al. 2006a; Carilli et al. 2010), but this is an observational, rather than a physical quantity. In this paper we choose to define the proximity region size as the scale length out to which the ionising flux from the quasar dominates over that from the background, i.e. where $\omega = 1$. As such any comparison between our proximity region sizes (values of R_{eq}) and those found by other methods for the same quasars should be made keeping this difference in mind. For further discussion on the distribution of proximity region sizes at high redshift see Maselli et al. (2009) and Bolton & Haehnelt (2007a).

A measurement of the UVB intensity can be expressed as a value of R_{eq} if the flux of ionising photons from the quasar and its fall-off with distance are known. We assume a $1/r^2$ fall-off, although possible deviations from this are discussed in Section 3.4.3. For this the flux at the Lyman limit, f_{ν_0} , needs to be determined. At the redshifts of the quasars discussed in this paper insufficient flux is transmitted through the forest for direct measurement of f_{ν_0} , and so we extrapolate the continuum flux (measured at a rest wavelength of 1280 \AA as described in Section 2.1) by assuming a power law relation of the form $f_{\nu} \sim \nu^{-\alpha}$. The value of α used in this paper is 1.61 ± 0.86 and is based on the $z < 2$ radio-quiet

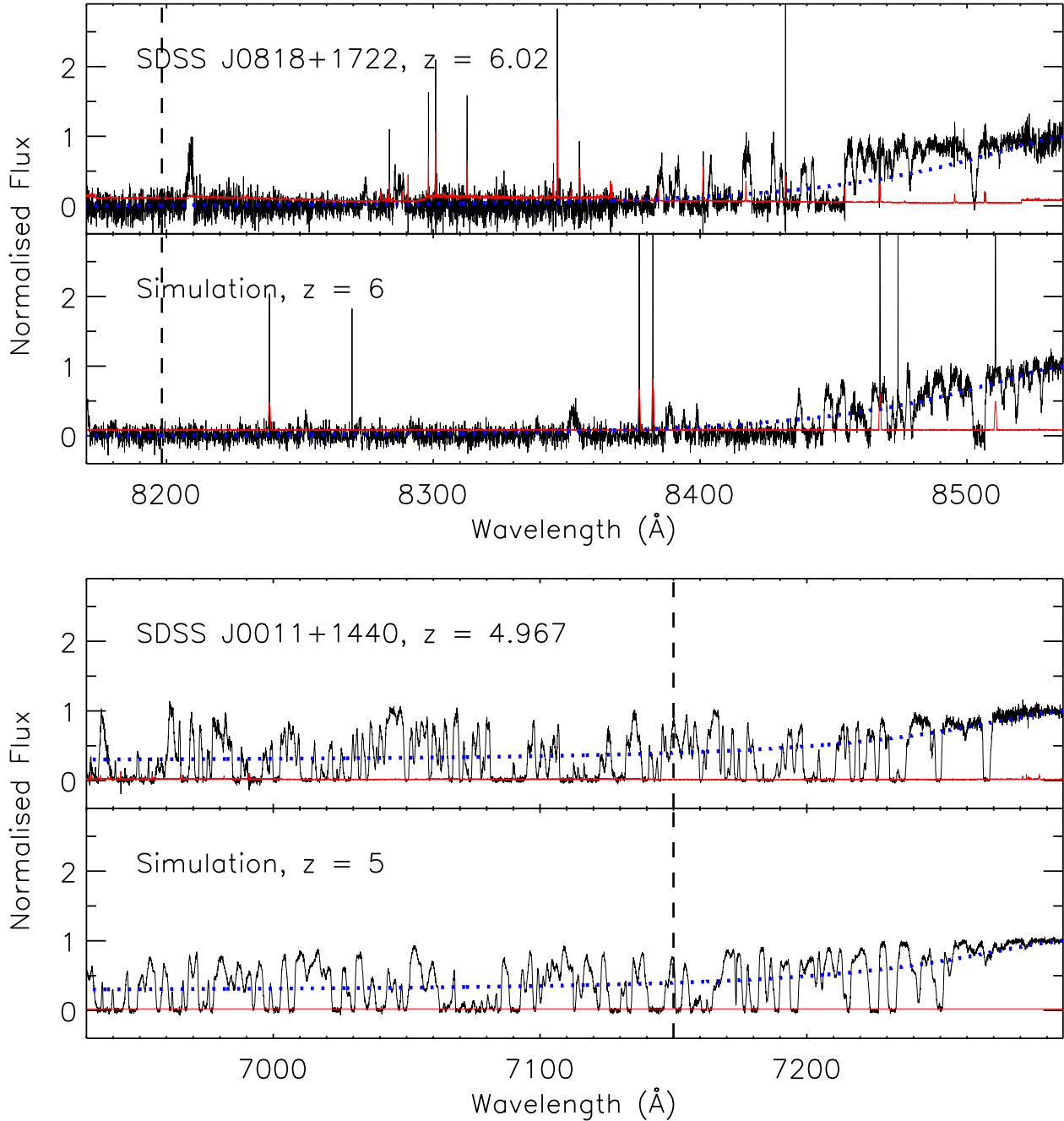


Figure 5. *Top:* The upper panel shows the normalised spectrum of SDSS J0818+1722 at $z = 6.02$, whilst the lower panel is a simulated spectrum at $z = 6$ with the same R_{eq} and Γ_{bkg} as presented in Table 5, as well as similar noise properties. The red solid line is the normalised error spectrum, the black dashed line is the derived value of R_{eq} , and the dotted blue line is the expected drop off in the mean normalised flux. Ly α at the redshift of the quasar is on the far right of each plot, and the simulated spectrum has been shifted so that it is at the same redshift as the observed spectrum. *Bottom:* The same as above but for SDSS J0011+1440 at $z = 4.967$ and the $z = 5$ simulation. Again there is a strong similarity between the two spectra. The value of R_{eq} is smaller at $z = 5$ than at $z = 6$ because the intensity of the UVB is higher, and so the ionising flux from the quasar dominates over the background out to a shorter distance.

quasar sample of Telfer et al. (2002), who measured this index in the range 500 to 1200 Å for 39 individual AGN. The error quoted is the RMS scatter of that sample. By contrast, Scott et al. (2004) found a harder index ($\alpha = 0.74$) in their $z < 0.67$ sample. The Scott et al. (2004) sample, however, covers a luminosity range that is an order of magnitude lower than either the Telfer et al. (2002) sample, or the quasars analysed here. The Telfer et al. (2002) mean

value and dispersion should therefore be the most appropriate for this study. Using f_{ν_0} , the luminosity of the quasar at the Lyman limit, L_{ν_0} , is calculated as

$$L_{\nu_0} = 4\pi d_L^2 \frac{f_{\nu_0}}{(1+z_q)}, \quad (5)$$

where d_L is the luminosity distance to the quasar. The quoted errors in L_{ν_0} take into account the error on α , the error in d_L (from the

Table 3. The contribution to the error and systematic shift in $\log(\Gamma_{\text{bkg}})$ from a variety of causes estimated from 1000 simulated spectra at $z = 5$ and $z = 6$, each with either $R_{\text{eq}} = 10$ or 5 proper Mpc. The errors from specified properties were found to have a nearly Gaussian distribution in $\log(\Gamma_{\text{bkg}})$. Each property, x_i , contributes an error σ_{x_i} and a systematic shift, ϵ_{x_i} (both measured in dex). The two instrumental resolutions represent those of MIKE and HIRES at $z = 5$ and $z = 6$ respectively. For the thermal proximity effect the temperature of the gas in the closest 5 proper Mpc has been raised by 10^4 K, similar to if the quasar had ionised He II (see Section 3.4.4). The total error is calculated by adding the individual errors in quadrature, whilst the total shift is the sum of the individual shifts. For comparison, we also simulated spectra with all possible sources of error included simultaneously (‘model’). The total error, as well as the total systematic shift, are similar to those expected from combining the individual effects.

Property	$z = 5$						$z = 6$					
	$R_{\text{eq}} = 10$ Mpc			$R_{\text{eq}} = 5$ Mpc			$R_{\text{eq}} = 10$ Mpc			$R_{\text{eq}} = 5$ Mpc		
	Value	σ_{x_i}	ϵ_{x_i}	Value	σ_{x_i}	ϵ_{x_i}	Value	σ_{x_i}	ϵ_{x_i}	Value	σ_{x_i}	ϵ_{x_i}
$\log L_{\nu_0}$	31.37	0.07	0.01	30.77	0.09	0.01	31.22	0.07	0.01	30.62	0.09	0.01
v_{pec}	-	0.09	0.05		0.12	0.05	-	0.04	-0.02		0.07	0.00
Sightline δF	21%	0.13	0.02		0.14	0.01	43%	0.10	0.02		0.13	0.02
$\Delta\tau_{\text{eff}}$	15%	0.22	0.03		0.23	0.01	30%	0.45	0.10		0.59	0.11
Δz	0.005	0.18	-		0.31	-	0.01	0.20	-		0.39	-
ΔL_{ν_0}	30%	0.14	-		0.14	-	30%	0.15	-		0.14	-
S/N	20	0.13	0.16		0.11	0.29	20	0.03	0.04		0.09	0.09
Inst. res.	13.6 km s ⁻¹	0.03	0.05		0.04	0.03	6.7 km s ⁻¹	0.02	0.01		0.04	0.00
Halo host mass	10 ¹³ M _⊙	0.10	0.12		0.16	0.33	10 ¹³ M _⊙	0.05	0.03		0.09	0.09
Thermal prox. effect	10 ⁴ K	0.07	-0.10		0.01	-0.17	10 ⁴ K	0.02	-0.11		0.09	-0.19
Total		0.41	0.33		0.51	0.57		0.54	0.08		0.76	0.13
Model		0.43	0.31		0.56	0.57		0.54	0.09		0.86	0.18

error in the redshift), and the error in the apparent magnitude of the continuum, m_{1280} . For quasars with $z_q < 5.5$ the error in m_{1280} is calculated from the error in the measured continuum flux for SDSS spectra as described in Section 2.1, whilst for those with $z > 5.5$ it is taken to be the same as the error on the SDSS z -band photometry. For a given distance from the quasar, r , the Lyman limit flux density is

$$F_{\nu_0}^{\text{Q}}(r) = \frac{L_{\nu_0}}{4\pi r^2}. \quad (6)$$

The photoionisation rate of H I (in units of s⁻¹) by a source of UV flux is given by

$$\Gamma = \int_{\nu_0}^{\infty} \frac{4\pi J(\nu)\sigma_{\text{HI}}(\nu)}{h\nu} d\nu, \quad (7)$$

where $J(\nu)$ is the intensity of the source, $\sigma_{\text{HI}}(\nu)$ is the ionisation cross-section of neutral hydrogen, and h is in this case Planck’s constant. By definition $J^{\text{bkg}}(\nu_0) = J^{\text{Q}}(\nu_0)$ at $r = R_{\text{eq}}$, and so using $\sigma_{\text{HI}}(\nu) = 6.3 \times 10^{-18} (\nu_0/\nu)^{2.75}$ cm² (Kirkman & Tytler 2008, note that the exponent is often approximated as 3) and integrating Equation 7 for the photoionisation rate by the background gives

$$\Gamma_{\text{bkg}} = \frac{9.5 \times 10^8 F_{\nu_0}^{\text{Q}}(R_{\text{eq}})}{(\alpha + 2.75)} \quad (8)$$

in units s⁻¹, where $F_{\nu_0}^{\text{Q}}(R_{\text{eq}})$ is the Lyman limit flux density in erg cm⁻² evaluated at a distance R_{eq} away from the quasar. Therefore, using Equation 6, Γ_{bkg} can be expressed as

$$\Gamma_{\text{bkg}} = \frac{9.5 \times 10^8 L_{\nu_0}}{(\alpha + 2.75)4\pi R_{\text{eq}}^2}, \quad (9)$$

where L_{ν_0} is in erg s⁻¹ Hz⁻¹ and R_{eq} is in cm.

3.2 Measurement method

The value of Γ_{bkg} was inferred for each quasar by increasing the optical depths of each pixel by the expected effect of the quasar,

using Equation 4, until the mean flux across the spectra was the same as that expected from the Ly α forest at that redshift. Details of this procedure are given below.

The analysis was carried out on the section of the spectrum immediately bluewards of the Ly α line and $40h^{-1}$ comoving Mpc ($\sim 8 - 9$ proper Mpc, or $\Delta z \sim 0.10 - 0.15$) in length. Each pixel is converted from a normalised flux into an optical depth using $\tau = -\ln(F)$. For a given quasar luminosity and trial value of Γ_{bkg} , Equation 9 can be inverted to give a trial value of R_{eq} . Using this trial value of R_{eq} , the factor $[1 + \omega(r)]^{-1}$ can be calculated for every pixel in the spectrum. The pixel optical depths are then adjusted, before being converted back into fluxes. This process is continued until the section of the spectrum resembles the Ly α forest at the same redshift. The most robust statistic for determining this was found to be the difference between the mean flux in the spectrum and the mean flux of the Ly α forest, F_{forest} . The difference between the two, ΔF , was defined as

$$\Delta F = \langle F_{\text{new}} \rangle - F_{\text{forest}}, \quad (10)$$

where $F_{\text{new}} = e^{-\tau_{\text{new}}}$ and $\tau_{\text{new}} = \tau[1 + \omega(r)]$. The value for which $\Delta F = 0$ we took as our estimate of Γ_{bkg} . The mean flux, $\langle F_{\text{new}} \rangle$, was calculated as a weighted mean, with each pixel weighted by the inverse variance of the flux. For a given original error in the transmission, σ_F , then $\sigma_{F_{\text{new}}} = \sigma_F [1 + \omega(r)]^{-1} F_{\text{new}}/F$. The weighted mean flux was then calculated as $\langle F_{\text{new}} \rangle = \sum (F_{\text{new}}/\sigma_{F_{\text{new}}}^2) / \sum (1/\sigma_{F_{\text{new}}}^2)$. In order to stop $\sigma_{F_{\text{new}}}$ from reaching zero and strongly biasing the weighting, a noise ‘floor’ was used such that $\sigma_{F_{\text{new}}} \geq 0.01$.

Trial values of $\log(\Gamma_{\text{bkg}})$ ranged from $-14 < \log(\Gamma_{\text{bkg}}) < -11$ and the iteration was done until a precision of 0.001 in $\log(\Gamma_{\text{bkg}})$ was reached. Fig. 1 shows the effect of the result of this iteration on simulated sightlines at $z = 5$ and $z = 6$. The ‘recovered’ Ly α forest (middle panels) is strikingly similar to the actual Ly α forest in those sightlines (bottom panels). Two observed spectra are presented in a similar fashion in Fig. 2. The bottom panels show the spectra after smoothing to mitigate the effect of pixel

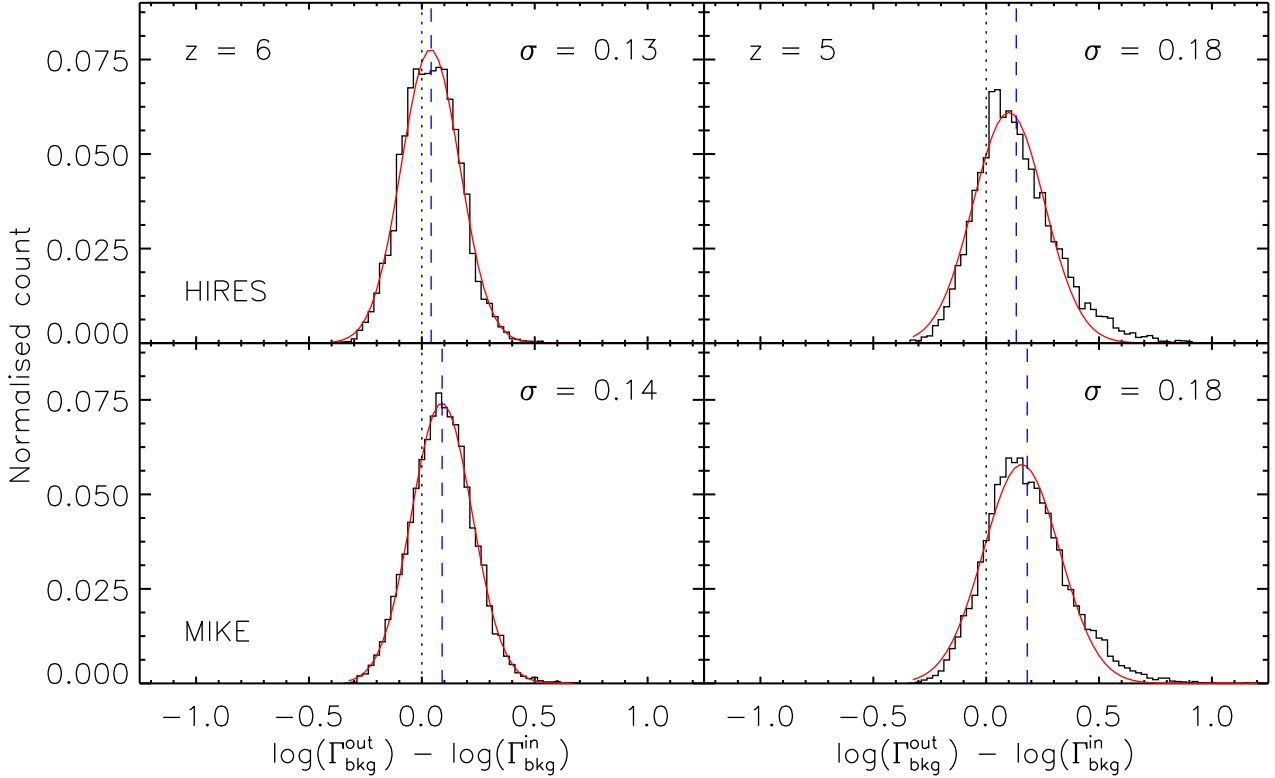


Figure 6. The deviation of the estimated value of $\log(\Gamma_{\text{bkg}})$ from the input value for 10 000 simulated spectra at $z = 6$ (left) and $z = 5$ (right) with input proximity regions of 10 proper Mpc in size. The spectra had a fixed $S/N = 20$, and the resolution of either the HIRES (top) or MIKE (bottom) spectrographs. The dotted black line marks the input value, whilst the blue dashed line marks the mean of the simulated data set. The spread is approximately Gaussian in $\log \Gamma$ with a small systematic offset caused by noise in the spectra. Each offset in the estimated Γ_{bkg} corresponds to an overestimate of the input value. The width of the Gaussian and size of the systematic offset varied with redshift, S/N , luminosity, and the resolution. Detailed modelling of the effect of each of these parameters was carried out to calculate the statistical error and bias in the estimated Γ_{bkg} for both individual quasars and a grouped sample. A detailed error budget is presented in Table 3, and more figures are presented in the Appendix.

noise (see Section 3.3) and after the optical depths have been modified using the estimated value of R_{eq} presented in Section 4.1.

The assumed value of F_{forest} is calculated at each redshift from the fit to measured optical depths of the Ly α forest in Becker et al. (2007). The fit is reproduced along with some observed values of τ_{eff} from the literature in Fig. 3. It assumes a simple evolution of a lognormal distribution of optical depths and matches the observed values excellently from $2 < z < 6$. Above $z = 6$ there are few measurements of the flux in the forest and so it is unknown if this relationship still holds. For the $z > 6$ quasars in this paper it was assumed that it does, although for large values of effective optical depth ($\tau > 6$), a substantial change in τ corresponds to only a very small (absolute) change in F_{forest} . Only a small change in R_{eq} , therefore, is required for ΔF to again be zero. This is apparent in Fig. 4, which shows an example of the results for one of the simulated spectra at $z = 5$ and at $z = 6$. If the mean flux is overestimated by a factor of 5, for example (corresponding to the dotted line being down at -0.10 and -0.010 in the top and bottom panels respectively) then the shift in the estimated $\log(\Gamma_{\text{bkg}})$ is much greater at $z = 5$ (~ 0.6 dex) than at $z = 6$ (~ 0.3 dex). The results from the $z > 6$ quasars should therefore be rather robust to significant uncertainties in the mean flux.

Probable skylines are identified as regions with $\sigma_F > 2 \langle \sigma_F \rangle$, where the mean is defined over the whole spectrum. Those pixels,

plus 5 pixels either side, are masked out. The data is also smoothed with a boxcar with a smoothing window that is proportional to the amount of noise in the data (window width = $10[\langle \sigma_F \rangle / 0.05]$ pixels), in order to balance between a smoothly varying function whilst maintaining some of the contrast and resolution in the proximity region. Regions with a smoothed flux below zero were treated as though they were positive, but remembering the sign, such that $F_{\text{new}} = -e^{-(-\ln |F|)[1+\omega(\tau)]}$. Smoothed fluxes that were greater than or equal to 1 (i.e. at the continuum) were set to be equal to 0.99. These effects, designed to limit the effects of observational artifacts, introduce a bias such that as the noise increases the method will systematically overestimate the UVB. These biases were therefore extensively modelled using the simulated spectra (see Appendix).

There are several advantages of our method over other recently presented methods to measure the intensity of the UVB from the proximity effect. One of the key attributes of our method is that the intrinsic distribution of Ly α optical depths need not be known *a priori*. This means that we are not directly dependent on numerical simulations. Another key advantage is that a slope, β , of the column density distribution of neutral hydrogen is not assumed, as was required in e.g. Dall’Aglio et al. (2008). We believe that with our method the largest remaining uncertainty is the evolution of τ_{eff} at $z > 6$.

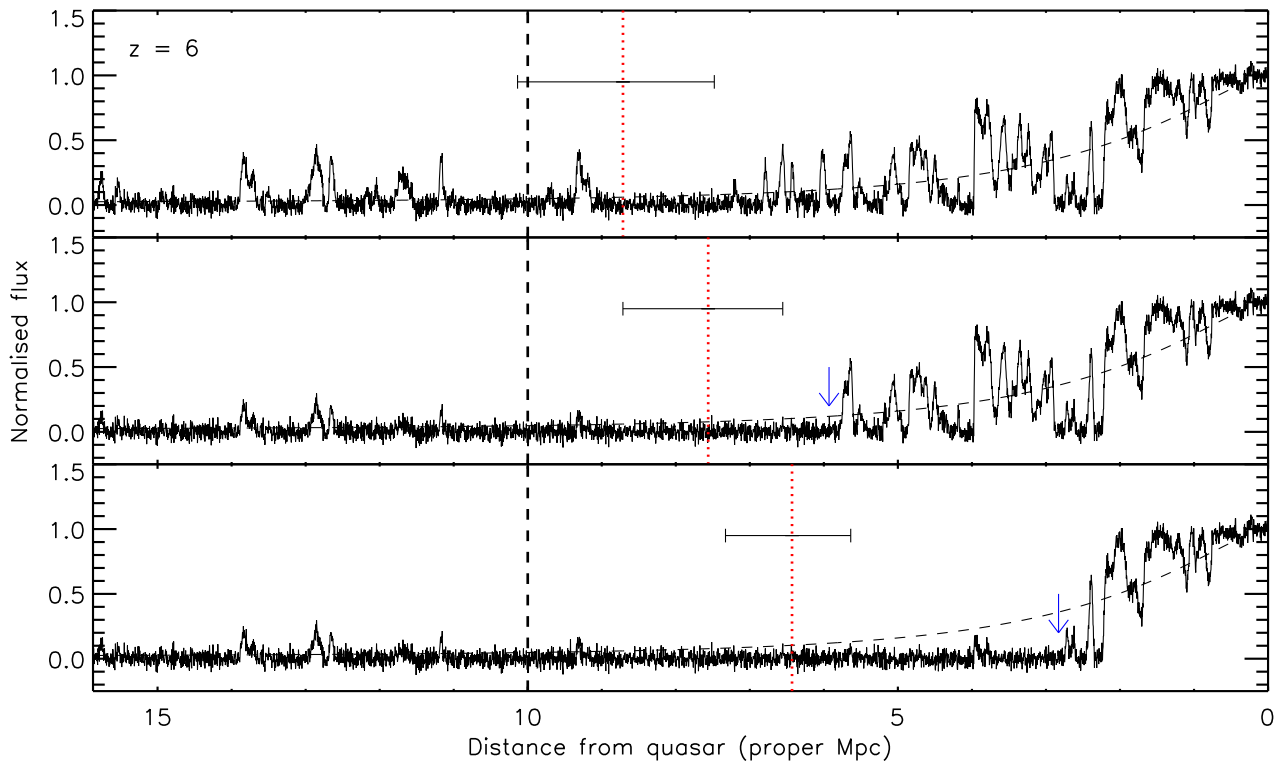


Figure 7. Demonstration of the impact of Lyman limit systems (see Section 3.4.3). *Top:* A standard simulated spectrum at $z = 6$ with $R_{\text{eq}} = 10$ proper Mpc and $S/N = 20$. The thick black dashed line marks this input R_{eq} whilst the dotted red line shows the one estimated by our method. The error bars correspond to the statistical error in the estimated R_{eq} , roughly 15 per cent. The thin black dashed line is the expected drop in normalised flux for the input R_{eq} . The method has, within error, recovered the input R_{eq} . *Middle:* The same spectrum as above, but with a Lyman limit system with corresponding $\text{Ly}\alpha$ absorption at the location of the blue arrow. The region of enhanced transmitted flux is slightly truncated, and so the estimated R_{eq} is slightly smaller than in the case of no Lyman limit system, corresponding to a higher estimated value of Γ_{bkg} . This is a well known bias in proximity effect measurements. *Bottom:* The same spectrum as in the top panel, but with the Lyman limit system much closer to the quasar, causing substantial shortening of the apparent size of the proximity region. There is again an associated decrease in the estimated R_{eq} , and thus a higher estimated Γ_{bkg} . However, the estimated values of R_{eq} are substantially more robust than would be expected from the extreme shortening of the apparent extent of the enhanced transmitted flux.

3.3 Statistical accuracy of the method

In order to test the accuracy of the method, simulated spectra were created using random sightlines through the simulations. The test spectra were all created using Model C at $z = 5$ and 6, and were $40h^{-1}$ (comoving) Mpc long, constructed by joining together multiple sightlines. In our standard mock spectra the proximity region was assumed to have a size of 10 proper Mpc. This is in general agreement with the derived values from the data (see Section 4.1) and that estimated by Wyithe & Loeb (2004). Assuming a Haardt & Madau (2001) UVB this corresponds to a quasar with $M_{1450} = -27.10$ (AB) at $z = 6$ and $M_{1450} = -27.47$ (AB) at $z = 5$. The noise was assumed to be Gaussian with a signal-to-noise (S/N) of 20, close to the average value of the S/N in the data.

In order to better mimic the real data, a variety of artifacts were introduced into the simulated spectra. Sky line residuals were added with an associated peak in the error spectrum, as well as bad pixels for which there was no associated effect on the error spectrum. Overall the simulated spectra are qualitatively very similar to the real data, as demonstrated in Fig. 5.

We applied our analysis to artificial spectra with similar S/N to the data. On average the method estimated the correct value of

Γ_{bkg} , with the distribution of values approximately Gaussian in $\log(\Gamma_{\text{bkg}})$. Several factors were thoroughly investigated for their effect on the size of the errors, and any bias on the estimated UVB intensity. We investigated the effects of peculiar velocities in the gas, v_{pec} , which will introduce distortions in redshift space to the expected radial profile of the transmitted flux. This was done by re-running our analysis on spectra generated with peculiar velocities set to zero. Similarly we examined the impact of sightline-to-sightline variations in the mean flux away from the global mean flux due to local fluctuations in the density field. For this we ran the analysis on spectra from which the mean flux of that sightline was known (equivalent to if the quasar was removed perfectly), and compared it to when simply assuming a global mean flux. The spread was also dependent on the noise levels in the simulated spectra, the redshift, the instrumental resolution, the luminosity, and the error in τ_{forest} (which varied with redshift). This analysis is shown in more detail in the Appendix. Each contributor to the error (see Table 3) was varied between reasonable limits for 1000 simulated spectra at both $z = 5$ and $z = 6$, and linearly extrapolated to other redshifts. This meant that the contribution to the error budget and associated bias from all the variables could be calculated for the parameter space and redshift range present in the data. Using this analysis an overall statistical error and bias were

determined for each individual quasar. For demonstration, the dependence on S/N and instrumental resolution is shown in Fig. 6. As expected, if the S/N decreases then the scatter in $\log(\Gamma_{\text{bkg}})$ increases. There is also a systematic bias, due to the smoothing of the spectra. Averaging over fluxes is not equivalent to averaging over optical depths, due to the non-linear relation between the two, and so the more the spectrum is smoothed the more the optical depths are underestimated. This effect is strongest for low fluxes (high optical depths). Consequently, smoothing (particularly at high redshift) increases the transmission in the forest so the fall-off in mean flux is not as steep. This corresponds to a smaller R_{eq} , and so ultimately $\log(\Gamma_{\text{bkg}})$ is overestimated. Since MIKE has a lower instrumental resolution than HIRES there is an additional bias brought in due to a similar effect. Indeed any effect that smoothes the spectra by averaging over pixel fluxes will bring in a bias of this nature. Table 3 breaks down the sources of scatter and systematic biases based on 1000 sightlines that have similar values to those in the data at $z = 5$ and $z = 6$. At both redshifts the errors are dominated by the error in τ_{eff} , and the errors in redshift are far more important than the errors in the luminosity. Even though the error in τ_{eff} is symmetric (it is approximated as a Gaussian), the resulting bias is asymmetric, and becomes more so at high τ_{eff} (i.e. high redshifts), as the equivalent distribution of F_{forest} also becomes highly asymmetric.

As we noted in Section 3.1 we assume a spatially uniform UVB. However, shortly after reionization has completed the mean free path of ionising photons is short enough that significant spatial variations in the UVB may exist (e.g. Lidz et al. 2007). Mesinger & Furlanetto (2009) show however that variations in the density field at $z \sim 5 - 6$ dominate over spatial variation in the UVB, and that even just after reionization assuming a uniform UVB underestimates Γ_{bkg} by at most a few percent. We thus do not try to correct for this uncertain but small effect.

We also performed a joint analysis of several sightlines simultaneously. These were modelled in a similar way, with the luminosities, noise properties and instrumental resolution equal to that of the component spectra in each bin being represented. From this a statistical error and bias could be determined for each bin.

The effect of other sources of systematic bias, such as Lyman limit systems (LLS, see Section 3.4.3), were also considered. These LLS are absorption features that are optically thick ($\tau > 1$) to Lyman limit photons, and so prevent the quasar from ionising as large a volume of the IGM as in their absence. Consequently they can truncate the extent of enhanced transmission in a spectrum. Fig. 7 demonstrates the case where a Lyman limit system has shortened the apparent proximity region. As the shortening becomes more severe, the method underestimates the true proximity region size (and thus overestimate the value of $\log(\Gamma_{\text{bkg}})$) as the LLS modifies the assumed $1/r^2$ fall-off from the quasar. However, our method is more resilient to this effect than previous proximity effect determinations of the UVB in the literature. Consequently it will produce on the whole more accurate values of UVB, less susceptible to the effects of Lyman limit systems. This is discussed in more detail in the following section.

3.4 Details of potential systematic biases

Whilst the proximity effect can be used on both individual sightlines (e.g. Williger et al. 1994; Cristiani et al. 1995; Lu et al. 1996) and in a statistical sense across many spectra (e.g. BDO; Cooke et al. 1997; Scott et al. 2000) to help constrain the redshift evolution of the UVB, several issues must be addressed before the

UVB estimates from the proximity effect can be considered robust. The proximity effect is essentially measuring the direct signature of an enhanced ionisation field near the quasar by noting a reduced fraction of H I extending out across a region of a few physical Mpc. Therefore any conversion from this physical size to a value for the UVB will be highly sensitive to any assumptions made about the quasar and its environment. There are three main systematic uncertainties in this conversion.

First, it is assumed that the quasar turned on a sufficiently long time ago that its proximity region is in photoionisation equilibrium with the IGM, and that it has been at its current luminosity over a similar timescale. The unknown level of variability in quasar luminosity on the order of 10^4 years (the timescales required for a region of the highly ionised IGM to reach ionisation equilibrium) means that the measured proximity region size may not correspond to a region in ionisation equilibrium, and so any measurement of the UVB may be biased (Pentericci et al. 2002; Schirber et al. 2004; Dall’Aglio et al. 2008).

The second problem is that in order to calculate an accurate size of the proximity region, an accurate systemic redshift for the quasar is needed. Redshifts determined from broad high-ionisation lines are underestimates of the systemic redshift (e.g. Richards et al. 2002), and an underestimate in the systemic redshift will cause the UVB to be overestimated (Espey 1993). It is worth noting, however, that an accurate systemic redshift can be determined from low ionisation lines, and so for some spectra this effect can be avoided. Also it should be noted that at high redshift the extent of enhanced transmitted flux will be larger than even the largest error in systemic redshift present in the data.

Finally, in the standard proximity effect analysis by BDO, the IGM within the proximity region is presumed to have the same density distribution as the IGM outside it. Quasars are however hosted by massive galaxies which are expected to reside in an environment which has higher than average density out to rather large distances (Granato et al. 2004; Fontanot et al. 2006; da Ângela et al. 2008). In that case, the proximity region would be smaller than expected for a region of the same size with an average density close to the global mean density (D’Odorico et al. 2008), and thus the UVB may be overestimated (Loeb & Eisenstein 1995). This environmental bias should be worst for the most luminous quasars which presumably lie in some of the most extreme overdensities at a given redshift (e.g. Pascarella et al. 2001; Adelberger et al. 2003; Kim & Croft 2007). As already discussed this is believed to be the main reason for the discrepancies between estimates of the UVB using the proximity effect and the flux decrement method (Rollinde et al. 2005; Guimarães et al. 2007; Faucher-Giguère et al. 2008) at redshift $z \sim 2 - 4$.

Another environmental effect that is often neglected is the consequence of the quasar heating the surrounding IGM via ionisation of He II. Bolton et al. (2010) found that the gas within ~ 5 proper Mpc of the $z \approx 6$ quasar SDSS J0818+1722 was $\sim 10^4$ K hotter than that presumed for the general IGM at that redshift. Higher temperatures within the proximity region will lead to more transmission, and so the UVB might then be underestimated.

All of these effects were investigated with the simulations at $z = 5$ and $z = 6$ to try and quantify how important they might be in the real data, and so each of these points will now be discussed in detail.

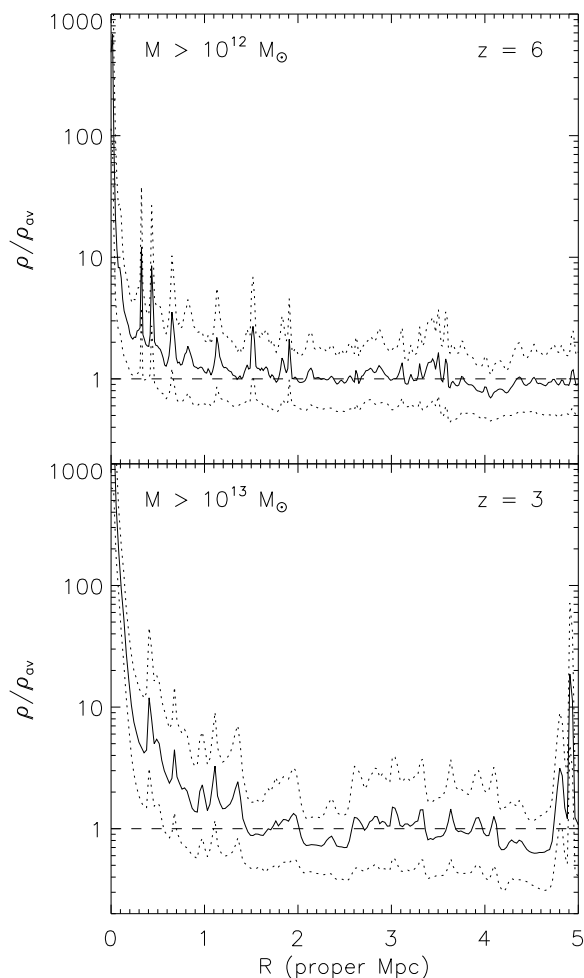


Figure 8. Mean density profiles around the most massive haloes in our simulation boxes. *Top:* The solid line is the average density field in the sightlines that start in haloes of masses greater than $10^{12} M_{\odot}$ in Model F at $z = 6$, plotted in proper Mpc. The dotted lines mark the $\pm 1\sigma$ deviations, and the mean density in the simulation is marked with the horizontal dashed line. Any significant overdensity is restricted to a region of ~ 1 Mpc in these haloes, and the overdense region will be even smaller for lower mass haloes. *Bottom:* The same as above but for haloes with mass greater than $10^{13} M_{\odot}$ at $z = 3$. These are essentially the same haloes as those at $z = 6$, but have become more massive through hierarchical growth. The overdense region is larger, extending out to ~ 3 Mpc, with evidence for smaller haloes clustered nearby (the small peak at ~ 5 Mpc). If the UVB is higher at this redshift then proximity region sizes will decrease, and may be comparable to the extent of the overdensity. In that case measurements of the size of the proximity region could depend strongly on the mass of the quasar host halo.

3.4.1 Effect of luminosity and redshift errors

Investigation with both the real and simulated spectra showed that the measured error on the UVB is dominated by errors in the redshift and the effective optical depth of the forest, and not by errors in the quasar luminosity. Even random errors in luminosity of up to 40 per cent had only a comparable effect to small errors (~ 0.01) in redshift. Of course, if the variability in quasar luminosity is not simply an extra source of random scatter, and in fact is instead systematic (for example, if the quasars are only observed in their brightest stages) then there will be a systematic bias as well as an additional

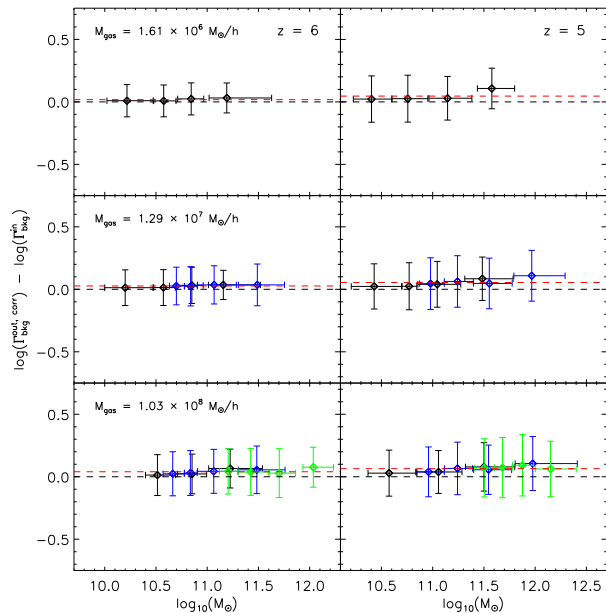


Figure 9. *Top row:* The ratio of the estimated Γ_{bkg} (corrected for systematic shifts due to noise) to the input Γ_{bkg} for sightlines starting in the 500 most massive haloes in the fiducial simulation, Model C. The proximity region in each spectra is 10 proper Mpc. On the left results are shown for $z = 6$ and on the right $z = 5$. The black dashed line is for zero bias, whilst the red line marks the true average value estimated. For these haloes there is a systematic overestimation of $\lesssim 0.1$ dex, but apparently no dependence on halo mass. *Middle row:* Same as above, but for Models B (black) and E (blue). Model B has been resampled to the same pixel size as Model E. *Bottom panel:* Same as above but for Models A (black), D (blue) and F (green). Due to the low resolution and small box size in Model A only 100 haloes could be identified at $z = 6$ and 250 haloes at $z = 5$. Models A and D have been resampled to the same pixel size as Model F. Lowering the mass resolution introduces a systematic overestimation in $\log(\Gamma_{\text{bkg}})$. This is due to the fact that the voids are under-resolved and so the proximity regions appear systematically smaller. The larger pixel sizes used in the lower mass resolution simulations also smooth the transmitted flux, so the proximity region is again underestimated (see Section 3.3). This effect is the stronger of the two. With these offsets taken into account, there is still no significant increase in Γ_{bkg} with halo mass, even in the bottom panel, which includes an $80h^{-1}$ comoving Mpc box with haloes of mass $> 10^{12} M_{\odot}$.

random error. The method ultimately is sensitive to the gradient of the fall-off in the mean transmitted flux throughout the spectrum, and so will give the same estimate for R_{eq} regardless of the quasar luminosity. Thus, if all the quasars are radiating at a systematically brighter luminosity than the one that established their proximity region, then the values of Γ_{bkg} will have been overestimated by the same amount, since they are linearly related in Equation 9.

Several of the quasars in this paper have a very accurate systemic redshift from either CO or Mg II emission lines (Carilli et al. 2010), and the high resolution spectra themselves allow for a reasonably accurate determination of the onset of the Ly α forest. Consequently almost all the redshift errors are ≤ 0.01 , corresponding to a size much smaller than the proximity region. We therefore believe that these two possible sources of error have been suitably dealt with.

3.4.2 Effect of quasars lying in overdensities

One of the more contentious assumptions used in proximity region measurements is that the environment of the quasar within the proximity region is similar to that of the general IGM. The quasar should lie in an overdense environment, and therefore could struggle to ionise as large a volume as it would in the general IGM, thus reducing the apparent size of the proximity region. As discussed already there have recently been a number of studies suggesting that proximity effect measurements may indeed suffer from a substantial bias due to this (Rollinde et al. 2005; Guimarães et al. 2007; Faucher-Giguère et al. 2008).

We have therefore tried to estimate how much such a bias may affect our measurements, which are at significantly higher redshift than previous studies. As a first attempt we looked into the effect of placing the quasar at the centre of massive dark matter haloes in our fiducial simulation and simulations with different box size and mass resolution.

For this we have chosen sightlines through the largest (by total mass) 500 haloes in Models B-F in 3 perpendicular directions through the box. Due to the low resolution and small box size of Model A, only 100 haloes could be identified at $z = 6$ and 250 at $z = 5$. For each halo the sightline was adjusted so that it began at the centre of a massive halo. Since the simulation box is cyclic the sightlines needed to be split in half so the sightline only passed through the overdensity once, and consequently for each halo 6 sightlines could be drawn (i.e. leaving the halo from both sides in 3 perpendicular directions). The halo sightlines were then spliced with random sightlines so that the total length of each spectrum was $40h^{-1}$ comoving Mpc. The proximity region size was chosen to be 10 proper Mpc, as in previous tests with the simulations. The results for the haloes in the fiducial simulation, Model C, are shown in the top panel of Fig. 9. There is no significant change as the mass increases, with a Gaussian spread in $\log(\Gamma_{\text{bkg}})$ in each bin of similar width to that from the random sightlines (Fig. 6).

The box size for Model C is, however, only $20h^{-1}$ comoving Mpc, which limits the maximum halo mass to just over $4 \times 10^{11} M_{\odot}$. Luminous quasars are likely to reside in host haloes more massive than this. The best observational constraints are inferred from the clustering analysis of quasars combined with predictions from Λ CDM simulations and suggest host halo masses in the range $10^{12} - 10^{13} M_{\odot}$ (e.g. Bonoli et al. 2009). It is important to note here that the very luminous quasars often used for proximity effect measurements are more luminous than those available for clustering analysis. It is thus perhaps not surprising that the proximity effect studies by Rollinde et al. (2005) and Guimarães et al. (2007) suggest that at $z \sim 2.5 - 4$ the host haloes of these very luminous quasars are even more massive. Fortunately, at the redshifts we consider here haloes more massive than $10^{13} M_{\odot}$ are not yet expected to have formed in large enough numbers to be credible candidates to host even the most luminous observed quasars (Springel et al. 2005; Sijacki et al. 2009). In order to probe overdensities around haloes in this mass range larger boxes are needed than we have considered so far, and so simulations with $40h^{-1}$ and $80h^{-1}$ comoving Mpc box size were also investigated. These were then compared with $20h^{-1}$ Mpc boxes with equal mass resolution. Model B was compared to Model E (see middle panel in Fig. 9), and Model A to Model D and Model F (bottom panel). Sightlines through Models A, B and D were resampled so that the pixel size (and mean forest flux) was the same as the largest simulation to which they were being compared. The highest mass bin in Model F ($> 10^{12} M_{\odot}$) still shows no more significant bias (in comparison to

less massive haloes in Models A and D), seeming to confirm the results from Model C that, at least at $z = 5 - 6$, the mass dependence of the bias is rather weak.

The largest halo mass in the $z = 6$ simulation was $10^{12.2} M_{\odot}$, which may still be nearly an order of magnitude less massive than the haloes the luminous quasars used in our study may reside in. To get a rough estimate of the effect of more massive haloes we have taken the density profile of haloes with $M > 10^{13} M_{\odot}$ at $z = 3$ in our simulation (the bottom panel in Fig. 8) and modified the optical depths of spectra created from random sightlines in the $z = 6$ simulation by using $\tau \propto \Delta^{2(\gamma-1)}$, where γ is from the temperature-density relation, $T(\Delta) \propto \Delta^{\gamma-1}$, and is taken to be 1.3. The extra systematic bias from such a massive halo is shown in Table 3. The effect is small at $z = 6$, and even though it is more important at $z = 5$, it is still not the main source of bias or main contributor to the error budget. Obviously this is just an approximation of how a halo this massive would affect the results, as the density profile was applied to the spectra artificially and will not be self-consistent with the other simulation outputs along the line-of-sight. However, since the effect is relatively minor we would not expect it to be a dominant source of error even if it were modelled self-consistently using a halo found in a much bigger simulation box. Since the quasars at $z = 6$ will probably lie in haloes with $M < 10^{13} M_{\odot}$ our estimate should be an upper limit of the effect of overdensities, and thus we conclude that at $z = 5 - 6$ the expected overdensity around our quasars is not critically important.

The most likely explanation for the lack of dependence of the bias of the UVB estimate on the mass of the host halo is that the proximity region is large in comparison to the size of the overdensity. This is demonstrated in Fig. 8 where the overdensity profile is shown at $z = 6$ and $z = 3$ for the largest haloes in Model F ($M > 10^{12} M_{\odot}$ and $M > 10^{13} M_{\odot}$ respectively). The gas will thereby tend to be infalling and the corresponding peculiar velocities will further decrease the apparent size of the proximity region in velocity space (Faucher-Giguère et al. 2008). In our simulated spectra the proximity regions were 10 proper Mpc, which is nearly an order of magnitude larger than the overdensity expected in the largest haloes at $z = 6$, and so the properties of the IGM within the proximity region should not be strongly biased due to the overdensity.

As a final point, we note that some clustering of galaxies and faint Active Galactic Nuclei (AGN) is expected around luminous quasars (e.g. Utsumi et al. 2010). The intensity of the UVB in the vicinity of luminous quasars could therefore be enhanced due to other nearby sources. Our knowledge about the clustering of faint AGN and galaxies around bright high-redshift quasars is rather sparse. We can nevertheless use the magnitudes and positions of the Lyman Break Galaxies (LBGs) found by Utsumi et al. (2010) for a rough estimate. In a field containing a quasar at $z = 6.43$ they found 7 LBGs at $z > 6.4$, based on their colours. Let us then calculate L_{ν_0} for each LBG from their z_R band magnitude, assuming they radiate isotropically, are all at the same redshift as the quasar, and have a ratio of far-UV to extreme-UV flux, $f_{1500}/f_{900} = 22$ (Shapley et al. 2006), as measured for $z \sim 3$ LBGs. With projected distances of 2 – 5 Mpc the LBGs would all lie within the typical proximity zones of our sample if they were indeed at the same redshift. Even if the LBGs would have a Lyman continuum as blue as we assume for the quasars (i.e. $\alpha = 1.61$) they would increase the size of the proximity region by as little as ~ 0.1 Mpc, and the UVB would typically be underestimated by 0.01 dex (3 per cent). There could obviously be a substantial contribution from more numerous fainter objects below the detection

Table 4. Summary of the parameters of the different power laws used to investigate the effect of LLS on both individual and grouped spectra. The number of expected LLS in a random sightline through Model C is calculated using Equation 11 with z_{\max} equal to the simulation redshift and $z_{\max} - z_{\min}$ corresponds to $20h^{-1}$ comoving Mpc. SC10 parameterise their power law with N_0 evaluated at $z = 3.5$ such that instead of $N(z) = N_0(1+z)^\gamma$ they have $N(z) = N_{3.5}[(1+z)/4.5]^\gamma$. The shifts, ϵ , quoted are the average overestimation in $\log(\Gamma_{\text{bkg}})$ due to the presence of LLS. For the individual spectra, those at $z = 6$ have HIRES resolution, and those at $z = 5$ have MIKE resolution. For the grouped spectra the shifts correspond to the $z \sim 5$ and $z \sim 6$ redshift bins, as described in Section 4.1. The final row represents the results based upon a power law consistent with the 1σ upper limit of the SC10 parameters.

	Redshift range	N_0	$N_{3.5}$	γ	n_{lls}	$z = 5$		$z = 6$		
						ϵ (ind)	ϵ (bin)	n_{lls}	ϵ (ind)	ϵ (bin)
SL94	$0.40 < z < 4.69$	$0.27^{+0.20}_{-0.13}$	–	1.55 ± 0.45	0.2169	0.15	0.09	0.3459	0.17	0.08
P03	$2.40 < z < 4.93$	$0.07^{+0.13}_{-0.04}$	–	$2.45^{+0.75}_{-0.65}$	0.2810	0.20	0.12	0.5146	0.26	0.11
SC10					0.2441	0.17	0.10	0.4134	0.22	0.09
SC10 1σ	$0 < z < 6$	0.15^a	2.80 ± 0.33	$1.94^{+0.36}_{-0.32}$	0.3022	0.21	0.12	0.5409	0.27	0.12

^a Derived from their $N_{3.5}$ and γ values.

limit. The faint end slope of the luminosity function of LBGs at $z \sim 6.4$ is not well constrained, but if we assume a slope of -1.73 (Bouwens et al. 2010) down to zero luminosity in the volume of the proximity region the UVB is still only underestimated by 0.04 dex (11 per cent). This is, however, likely to be an upper limit, as in reality the 7 LBGs do not have precise redshifts and may not be within the proximity region of the quasar. This should outweigh the possibility that the galaxies may have a larger value of f_{1500}/f_{900} than we have assumed here. We therefore conclude that the effect of nearby LBGs could be noticeable but appears likely to be small. Considering the large uncertainties in our rough estimate we did not try to correct for this.

3.4.3 Effect of Lyman limit systems

Lyman limit systems (LLS) are due to regions of neutral gas that are optically thick ($\tau > 1$) to Lyman limit photons ($\lambda_{\text{rest}} = 912 \text{ \AA}$), which corresponds to a hydrogen column density of $N(\text{H I}) > 1.6 \times 10^{17} \text{ atom cm}^{-2}$. Should a LLS lie in the observed line-of-sight of the quasar then the apparent size of the proximity region will be shortened, as their abundance limits the mean free path of ionising photons (e.g. Storrie-Lombardi et al. 1994; Miralda-Escudé 2003; Péroux et al. 2003; Furlanetto & Mesinger 2009).

Studies counting the number of LLS in spectra struggle at high redshift as, due to the ever increasing blackness of the forest, features with $\tau > 1$ are difficult to detect. Consequently there are very few studies that provide measured LLS frequency at the redshifts covered in this paper. LLS can lead to dramatic shortening of the region of enhanced transmission (see Fig. 7) and so if abundant at high redshift then they could be a substantial source of systematic errors.

We inserted LLS into our simulations following the method presented in Appendix D of Bolton & Haehnelt (2007a). A density threshold, ρ_{thresh} , was chosen such that the average number of regions in a spectrum with $\rho \geq \rho_{\text{thresh}}$ was the same as a given number of LLS expected per sightline. The neutral fraction within those regions was then set to unity (i.e. they become self-shielded). As such, they absorb all the ionising flux of the quasar so further out in the spectrum the transmission in the forest is from the UVB alone. The expected number of LLS in a particular sightline, n_{lls} , was calculated from the power laws presented by Storrie-Lombardi et al. (1994), Péroux et al. (2003), and Songaila & Cowie (2010), (hereafter SL94, P03 and SC10 respectively), where $N(z) \equiv dN/dz = N_0(1+z)^\gamma$. SL94 used quasars

covering the range $0.40 < z < 4.69$, and suggest that for a sightline covering the redshift range z_{\max} to z_{\min} that

$$n_{\text{lls}} = \int_{z_{\min}}^{z_{\max}} N_0(1+z)^\gamma, \quad (11)$$

where $N_0 = 0.27$ and $\gamma = 1.55$. For a particular random sightline in Model C z_{\max} was taken to be the redshift of the simulation and $z_{\max} - z_{\min}$ corresponds to the simulation box size. This meant that $n_{\text{lls}} = (0.2169, 0.3459)$ at redshift $z = (5, 6)$ respectively. From this (using only the random sightlines) the threshold densities were derived as $\log(\Delta_{\text{thresh}}) = (1.6310, 1.4080)$ (where $\Delta_{\text{thresh}} \equiv \rho_{\text{thresh}}/\rho_{\text{av}}$) and those regions were then presumed to be self-shielded. Similar calculations were also done for the power laws of P03 and SC10, and a worst case scenario was investigated using the 1σ upper limits of SC10. The expected overestimations in $\log(\Gamma_{\text{bkg}})$ for each of these power laws are presented in Table 4 for both individual spectra, and grouped spectra. Consequently, assuming the predictions of SC10 to be the most reliable as this is the only study probing the redshift range we are interested in, the effect would be to shift the results of the individual quasars down by 0.17 (0.22) dex at $z = 5$ (6), and possibly up to 0.21 (0.27) dex.

SC10 is the only study into the actual spatial frequency of LLS at $z = 6$. In both SL94 and P03 they found that towards higher redshifts, $N(z)$ starts to evolve rapidly, and so extrapolations become much more uncertain. Indeed Prochaska et al. (2010) note that both of those papers are subject to biases that they claim have not been adequately compensated for, and so they may have overestimated $N(z)$ by up to a factor of 3. Clearly if n_{lls} is a factor of 3 smaller then the effect on Γ_{bkg} would be greatly reduced. SC10 themselves also warn against extrapolating to $z > 6$ due to the potential rapid change in the mean free path of ionising photons if reionization is being probed. Taking all these factors into account, and treating SC10 as the most reliable power law, we cautiously estimate using their 1σ upper limits on n_{lls} that the binned data points in Fig. 13 are possibly overestimated by ≤ 0.12 dex.

3.4.4 Effect of quasars heating the IGM in the proximity region

We have implicitly assumed that the temperature of the quasar proximity region is comparable to that of the general IGM. This may be not true, particularly prior to He II reionization, when the ionisation of He II by the quasar may heat the local IGM (e.g. Bolton et al. 2010). This temperature gradient will cause higher mean flux in the proximity region, and so the proximity region size will be *overestimated* and the UVB *underestimated* (i.e. opposite to all the other environmental biases). We constructed a toy

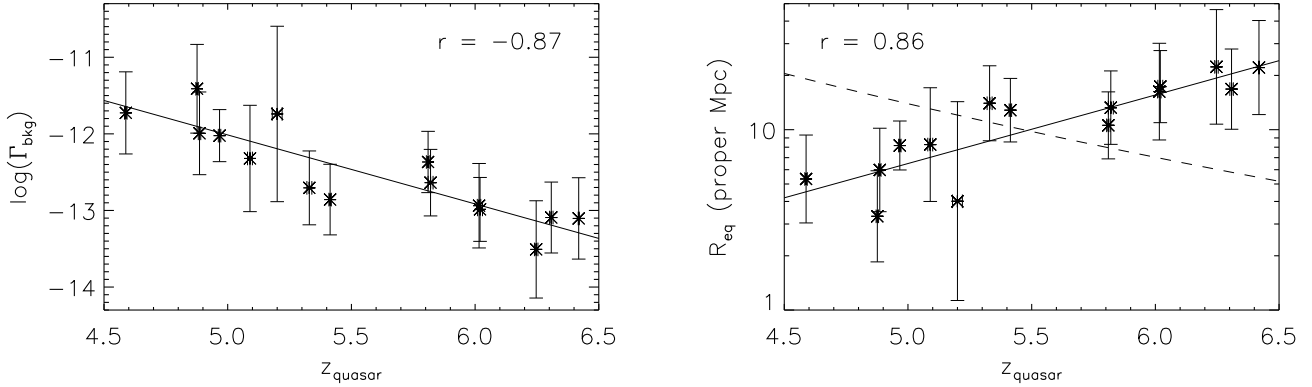


Figure 10. *Left panel:* The bias corrected estimates of $\log(\Gamma_{\text{bkg}})$ for the 15 individual quasars studied in this paper. The errors are calculated as the standard deviation in $\log(\Gamma_{\text{bkg}})$ from 10 000 Monte Carlo realisations (varying the systemic redshift, luminosity and forest τ_{eff}) added in quadrature to the statistical error, which was individually calculated for each quasar sightline. Biases similar to those listed in Table 3 have also been removed. A smooth decline in Γ_{bkg} with redshift appears over this redshift range, with a formal correlation coefficient of -0.87 . *Right panel:* The inferred values of R_{eq} for each quasar. The error bars were calculated in the same way as those for Γ_{bkg} . There is a strong increase towards higher redshifts, driven by the declining intensity of the UVB. A fit to this increase is shown by the solid line, and the formal correlation coefficient is 0.86 . The dashed line marks the evolution in the mean free path of ionising photons from the formula in Songaila & Cowie (2010). The size of the proximity region is larger than the mean free path at $z \gtrsim 5.5$. The implications of this are discussed in Section 4.2.

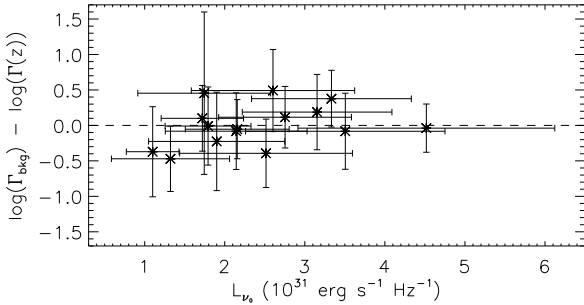


Figure 11. Plot of the deviance from the linear fit to $\log(\Gamma_{\text{bkg}})$ in the left panel of Fig. 10 against the quasar luminosity. The dashed line marks zero deviation. All of the points are consistent with this line, which suggests that the measured values of $\log(\Gamma_{\text{bkg}})$ have been adequately corrected for systematic biases from quasar luminosities.

model in the simulations with the change in temperature as a step function, such that the gas within 5 proper Mpc of the quasar was 10^4 K hotter than that in the general IGM. This is similar to the result of Bolton et al. (2010), assuming general IGM temperatures at $z = 5 - 6$ of $\sim 10^4$ K (Becker et al. 2010). In individual sightlines this caused $\log(\Gamma_{\text{bkg}})$ to be underestimated by 0.10 (0.11) dex at $z = 5$ (6), and in the binned data by 0.14 (0.21). Consequently, we find that the hotter temperatures of gas close to the quasar could cause underestimation in $\log(\Gamma_{\text{bkg}})$ comparable to the overestimations from other environmental effects at the redshifts of our study.

4 RESULTS AND DISCUSSION

4.1 Results

Table 5 summarises the main results of this paper for the individual quasar sightlines. The quoted errors in Γ_{bkg} consist of the measured error from 10 000 Monte Carlo realisations of the spec-

tra, varying the luminosity, systemic redshift and forest τ_{eff} , added in quadrature to the expected sightline-to-sightline scatter as described in Section 3.3. The spectra with the largest errors in $L_{\nu_0}^{\text{Q}}$ are those with continuum magnitudes measured directly from the SDSS spectra. Even though the errors in the luminosity could be rather large (~ 30 per cent), the measured error was strongly dominated by errors in the redshift and τ_{eff} . The statistical power of a measurement from a single spectrum is rather limited and the error on Γ_{bkg} is substantial. Fig. 10 shows the estimated $\log(\Gamma_{\text{bkg}})$ and R_{eq} for our sample as a function of redshift. The data points in Fig. 10 are consistent with a linear fit within the errors. There is therefore little we can say about spatial fluctuations in UVB intensity other than that they appear to be smaller than our measurement errors. We note that if we had used the α presented in Scott et al. (2004) then the $\log(\Gamma_{\text{bkg}})$ values would have been on average 0.22 dex higher, and the error bars 10 per cent larger. We also note that our redshift evolution of R_{eq} is opposite to the redshift evolution of the proximity region sizes as presented by Fan et al. (2006a). Note that this is entirely due to the different definition of the two sizes considered. For the proximity region size definition from Fan et al. (2006a) we find similar results.

In Fig. 11 we subtract out the linear evolution of the average $\log(\Gamma_{\text{bkg}})$. There is no systematic trend with the luminosity of the quasar. This confirms that the systematic shifts induced by the luminosity of the quasar (see Table 3 and Fig. A5) have been suitably corrected for. Fig. 12 shows a sample of the observed spectra with their derived R_{eq} and expected average flux fall-off, in their rest frame, as well as denoting the section of each spectrum used for the measurement. Judging by visual inspection, none of our observed spectra appears to be influenced by LLSs to the degree presented in the bottom panel of Fig. 7. It is, however, difficult to determine if any of the sightlines contained LLSs far from the quasar redshift, as in the middle panel of Fig. 7. SDSS J1148+5251 has a very short region of enhanced transmitted flux (Fig. 12) and is a possible candidate for being affected by a LLS.

Our most robust results come from simultaneously fitting multiple sightlines. The data were grouped into low redshift ($z < 5.5$)

Table 5. Tabulated results for each of the investigated quasar sightlines. Those with σ_z of 0.002 or 0.007 have systemic redshift taken from the CO or Mg II emission lines (Carilli et al. 2010) while the others use either the Ly α + N V emission line redshift, or (in most cases) use the redshift at which the Ly α forest appears to begin. Due to the high-resolution of the spectra, errors for these are ≤ 0.01 . The absolute magnitudes at rest-frame 1450 Å were calculated from either the published continuum magnitudes (Fan et al. 2001, 2003, 2004, 2006b) or the measured fluxes at rest-frame 1280 Å, extrapolated to 1450 Å by assuming a power law continuum of the form $f_\nu \propto \nu^{-0.5}$.

Name	z_q	σ_z	z source	$L_{\nu_0}^Q$ $10^{31} \text{ erg s}^{-1} \text{ Hz}^{-1}$	M_{1450} (AB)	R_{eq} (Mpc)	Γ_{bkg} 10^{-12} s^{-1}	$\log(\Gamma_{\text{bkg}})$
SDSS J1148+5251	6.4189	0.002	CO	3.154 ± 0.935	-27.81	$22.1^{+18.2}_{-10.0}$	$0.08^{+0.19}_{-0.06}$	-13.10 ± 0.53
SDSS J1030+0524	6.308	0.007	Mg II	1.721 ± 0.516	-27.15	$16.8^{+11.2}_{-6.7}$	$0.08^{+0.15}_{-0.05}$	-13.09 ± 0.46
SDSS J1623+3112	6.247	0.007	Mg II	1.100 ± 0.329	-26.67	$22.3^{+24.0}_{-11.6}$	$0.03^{+0.10}_{-0.02}$	-13.51 ± 0.64
SDSS J0818+1722	6.02	0.01	Ly α forest	2.156 ± 0.649	-27.40	$17.3^{+10.1}_{-6.4}$	$0.10^{+0.17}_{-0.06}$	-12.99 ± 0.42
SDSS J1306+0356	6.016	0.007	Mg II	1.792 ± 0.536	-27.20	$16.3^{+13.9}_{-7.5}$	$0.12^{+0.30}_{-0.08}$	-12.94 ± 0.55
SDSS J0002+2550	5.82	0.01	Ly α forest	2.754 ± 0.829	-27.67	$13.3^{+7.9}_{-5.0}$	$0.23^{+0.40}_{-0.15}$	-12.64 ± 0.43
SDSS J0836+0054	5.810	0.007	Mg II	3.333 ± 0.998	-27.87	$10.6^{+5.6}_{-3.7}$	$0.43^{+0.65}_{-0.26}$	-12.37 ± 0.40
SDSS J0231-0728	5.41	0.01	Ly α forest	1.323 ± 0.738	-26.87	$12.8^{+6.4}_{-4.3}$	$0.14^{+0.26}_{-0.09}$	-12.86 ± 0.46
SDSS J1659+2709	5.33	0.01	Ly α forest	2.516 ± 1.079	-27.57	$14.0^{+8.6}_{-5.3}$	$0.20^{+0.40}_{-0.13}$	-12.71 ± 0.48
SDSS J0915+4924	5.20	0.02	Ly α + N V	1.744 ± 0.830	-27.17	$4.0^{+10.3}_{-2.9}$	$1.82^{+23.60}_{-1.69}$	-11.74 ± 1.15
SDSS J1204-0021	5.09	0.01	Ly α forest	1.900 ± 0.851	-27.26	$8.3^{+8.8}_{-4.3}$	$0.48^{+1.88}_{-0.38}$	-12.32 ± 0.69
SDSS J0011+1440	4.967	0.005	Ly α forest	4.518 ± 1.604	-28.20	$8.2^{+3.0}_{-2.2}$	$0.95^{+1.13}_{-0.52}$	-12.02 ± 0.34
SDSS J2225-0014	4.886	0.005	Ly α forest	2.144 ± 0.885	-27.39	$6.0^{+4.2}_{-2.5}$	$1.02^{+2.51}_{-0.72}$	-11.99 ± 0.54
SDSS J1616+0501	4.876	0.005	Ly α forest	2.603 ± 1.020	-27.60	$3.3^{+2.6}_{-1.5}$	$3.89^{+10.80}_{-2.86}$	-11.41 ± 0.58
SDSS J2147-0838	4.588	0.005	Ly α forest	3.506 ± 1.245	-27.93	$5.3^{+4.0}_{-2.3}$	$1.88^{+4.58}_{-1.33}$	-11.73 ± 0.54

and high redshift ($z > 5.5$) samples, and Γ_{bkg} was measured by finding where $\sum_i \Delta F_i = 0$, with ΔF calculated for each spectrum using the same trial Γ_{bkg} . For the lower redshift bin, containing 8 spectra, the average redshift was $z = 5.04$ and gave $\log(\Gamma_{\text{bkg}}) = -12.15 \pm 0.16$ (0.32) at 68 (95) per cent confidence, whilst for the higher redshift bin with 7 spectra and an average redshift of $z = 6.09$, $\log(\Gamma_{\text{bkg}}) = -12.84 \pm 0.18$ (0.36). These will subsequently be referred to as the $z \sim 5$ and $z \sim 6$ samples, respectively, for ease of comparison to the simulations and previous work. The implications of these results will now be discussed.

4.2 Comparison to previous work

The results of fitting multiple lines of sight with a constant UVB are plotted in Fig. 13. We also plot a selection of UVB estimates from the literature, where the literature results have been scaled to the cosmology used in this paper, as well as the same temperature-density relation parameters used by Bolton & Haehnelt (2007b), such that $T = T_0 \Delta^{\gamma-1}$, with T_0 and γ held constant at 10^4 K and 1.3 respectively. The UVB model of Haardt & Madau (2001) is also shown. As previously noted in Fig. 10, whilst the error bars are large for the individual sightlines, there is a clear trend of a decreasing UVB intensity in the redshift range $z \sim 5 - 6$. This decrease is more pronounced in the binned results.

The results presented here are the first proximity effect measurements of Γ_{bkg} at these redshifts. Dall’Aglio et al. (2009) detected the proximity effect in 1733 spectra from the SDSS over the range $2 \lesssim z \lesssim 4.5$ and found that the UVB seemed to be remarkably flat over this redshift range, with $\log(\Gamma_{\text{bkg}}) = -11.78 \pm 0.07$. This value is consistent with our results from individual sightlines over $4.5 < z < 5$. A more direct comparison can be made with the results of Dall’Aglio et al. (2008), who measured the proximity effect in 40 spectra from the UVES instrument on the VLT. Comparing our results to the Dall’Aglio et al. (2008) results may be more appropriate, as both studies used high-resolution spectra.

Combined, the proximity effect results suggest a smooth decrease in UVB from $z \sim 2$ to $z \sim 6$ by an order of magnitude (Fig. 13).

The range $z \sim 5 - 6$ has previously only been probed using flux decrements (McDonald & Miralda-Escudé 2001; Meiksin & White 2004; Bolton & Haehnelt 2007b; Wyithe & Bolton 2010). There is excellent agreement between our binned results and those from flux decrements (see Fig. 13), which also suggest a significant decline in the UVB from $z \sim 4$ to $z \sim 6$.

Our measured evolution of the UVB intensity has important implications for reionization. The H I photoionisation rate should scale as $\Gamma(z) \propto l(\nu_0, z) \epsilon_{\nu_0}$, where $l(\nu_0, z)$ is the mean free path of ionising photons and ϵ_{ν_0} is the ionising emissivity. The redshift evolution of Γ_{bkg} therefore gives an insight into the evolution of these two key variables. During the ‘percolation’ stage at the end of reionization, $l(\nu_0, z)$ is expected to evolve rapidly, in marked contrast to its gradual evolution in the post-reionization Universe (Gnedin & Fan 2006). Consequently, the end of reionization should be indicated by a break in the evolution of $l(\nu_0, z)$. The smooth redshift evolution of our measurements of the UVB intensity (see left panel of Fig. 10) implies that both $l(\nu_0, z)$ and ϵ_{ν_0} are also evolving smoothly in the redshift range $4.6 < z < 6.4$, as otherwise they would have to both evolve rapidly simultaneously in opposite directions, which appears very unlikely. This suggests that percolation has occurred at higher redshifts than are probed by our sample (although see Furlanetto & Mesinger 2009).

Our measurements of the UVB can be combined with measurements of the mean free path to place constraints on the evolution of the ionising emissivity. Songaila & Cowie (2010) recently measured the incidence of LLS over $0 < z < 6$. They find an evolution in the mean free path which can be approximated as $l(\nu_0, z) = 50[(1+z)/4.5]^{-4.44^{+0.36}_{-0.32}}$. Using this fit, we infer that $l(\nu_0, z)$ decreases by a factor $\sim 1.5 - 2.5$ from $z = 5 - 6$. At face value the decrease of our measurements of Γ_{bkg} with redshift (a factor of $\sim 2.5 - 8$) therefore imply an emissivity that is either roughly constant or drops by up to a factor of ~ 5 . Note that this is consistent with the decrease in the (dust-corrected) UV luminos-

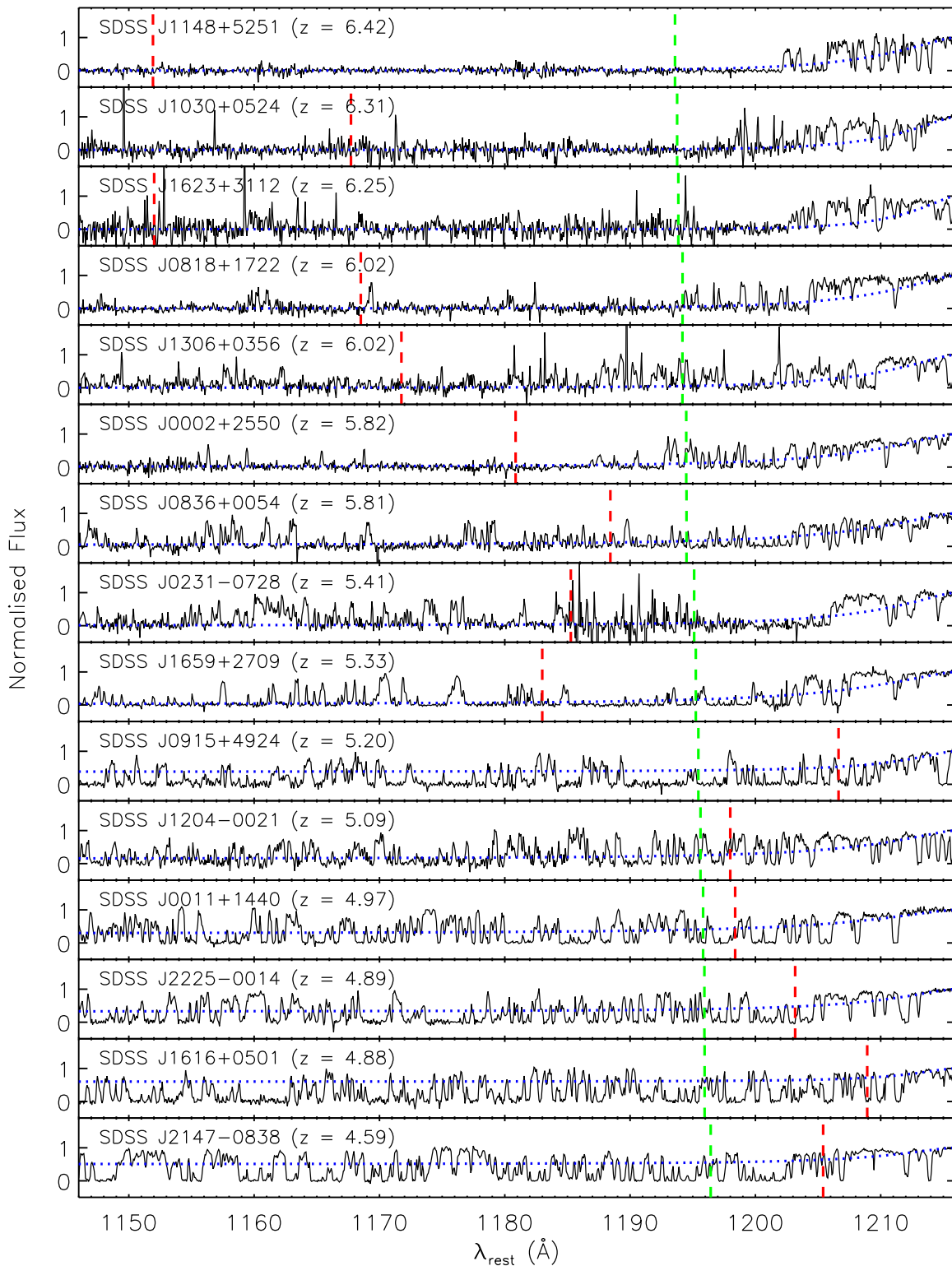


Figure 12. The 15 spectra used in this study, ordered by redshift. The spectra are presented in their rest wavelength, λ_{rest} , in order to emphasise the proximity effect region bluewards of the Ly α emission line, on the far right of the plot at 1216 Å. They have been normalised with the continuum fitting process described in Section 2.1, and have also been smoothed to a common pixel size of 16.7 km s $^{-1}$ (observed frame) for clarity. The red dashed line indicates the derived value of R_{eq} , whilst the blue dotted line is the expected fall-off in average flux. The area of spectrum to the right of the green dashed line was the section used for the proximity effect measurement, and is $40h^{-1}$ comoving Mpc long.

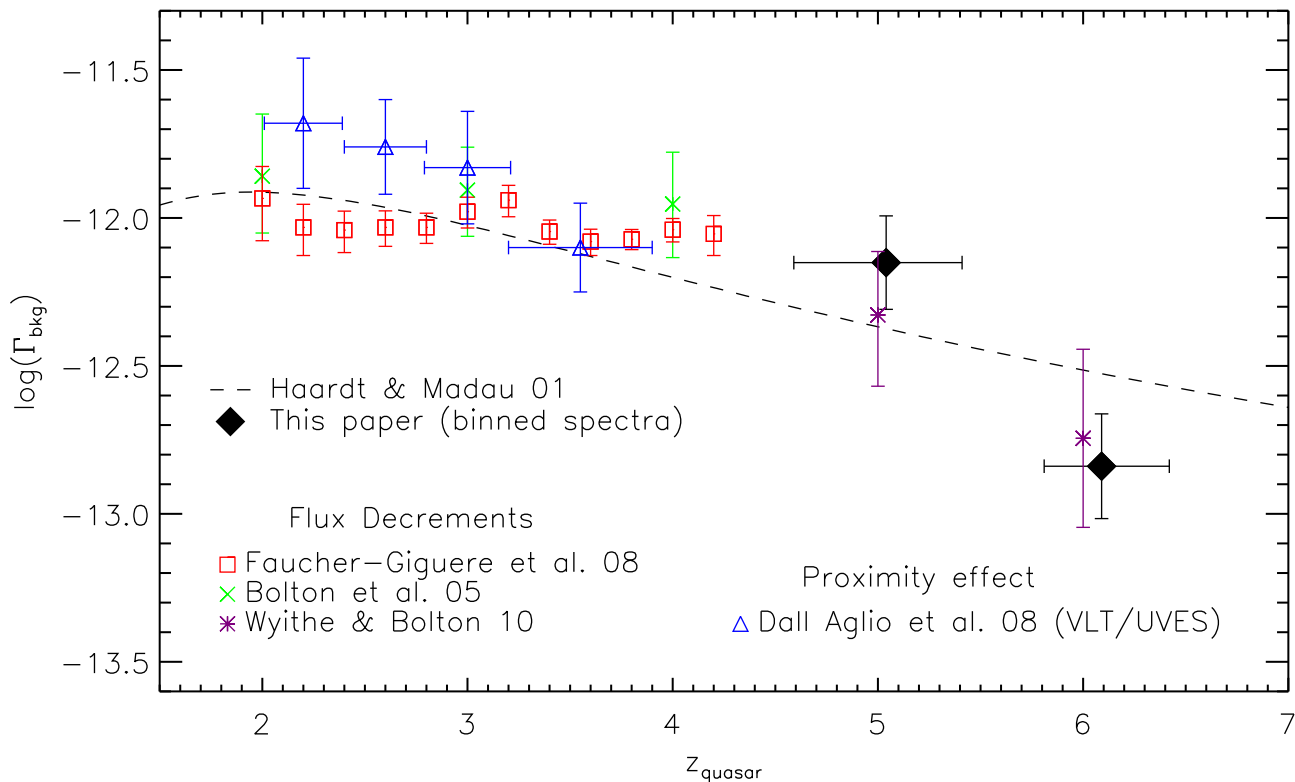


Figure 13. The evolution of the UVB in the redshift range $z = 2$ to $z = 6$. The solid points are the results of this paper, and represent the aggregate analysis over multiple sightlines. The spectra were coarsely binned into two subsets, namely $z > 5.5$ and $z < 5.5$. The lower redshift subset contained 8 spectra and had an average redshift of $z_{\text{av}} = 5.04$ whilst the upper had 7 spectra and $z_{\text{av}} = 6.09$. The errors displayed on our points are the 68 per cent confidence intervals, and exclude any correction due to the presence of LLS, local overdensities, or a thermal proximity effect. Recent estimates from the literature are also plotted with their 1σ errors. The flux decrement results have all been scaled to our adopted cosmology $(h, \Omega_m, \Omega_b h^2, \sigma_8) = (0.72, 0.26, 0.024, 0.85)$ and to the same temperature-density relation, $T = T_0 \Delta^{\gamma-1}$, with T_0 and γ held constant at 10^4 K and 1.3 respectively, using the scaling relations from Bolton et al. (2005) and Bolton & Haehnelt (2007b). Our results at both $z \sim 5$ and $z \sim 6$ agree very well with those from flux decrement measurements. The theoretical curve of Haardt & Madau (2001), assuming contributions from quasars and star forming galaxies, is also plotted.

ity density between $z = 5 - 6$ measured by Bouwens et al. (2009) for rest wavelength $\sim 1600 \text{ \AA}$ and integrated to either $0.3L_{z=3}^*$ or $0.04L_{z=3}^*$ (where $L_{z=3}^*$ is the luminosity derived by Steidel et al. (1999) at $z \sim 3$ and corresponds to $M_{1700,AB} = -21.07$).

The fit to the mean free path from Songaila & Cowie (2010) is plotted with the measured proximity region sizes in the right panel of Fig. 10. Our proximity region sizes become larger than the mean free path as measured by Songaila & Cowie (2010) at $z \gtrsim 5.5$. If the quasar is able to ionise LLS within the proximity region, then the mean free path within the proximity region will increase, allowing an enhanced contribution to the ionisation rate from local galaxies and AGN. As a result, the proximity region may appear larger, and so the UVB may be underestimated in a proximity effect analysis. Careful modeling of LLS will be required to determine whether this is an important effect. However, it may partly explain the decrease in ionising emissivity we infer from $z \sim 5$ to 6 (see also Section 3.4.2).

The ionising emissivity is already very low at $z = 6$ (~ 1.5 ionising photons per hydrogen atom) and so this evolution can not continue to much higher redshifts without reionization failing to complete by $z = 6$ (Bolton & Haehnelt 2007b). For this reason, unless there is a substantial increase in ϵ_{ν_0} at very high redshifts,

the end of reionization, while potentially before $z = 6.4$, appears unlikely to occur much earlier.

5 CONCLUSIONS

We have presented new measurements of the photoionisation rate of hydrogen by the ultraviolet background (UVB) using the proximity effect in quasar spectra. The fifteen spectra in the sample cover the range $4.6 < z < 6.4$, allowing us to conduct the first proximity effect measurements of Γ_{bkg} at these high redshifts.

For each quasar, Γ_{bkg} was calculated by modelling the total photoionisation rate as a function of distance from the quasar, taking into account contributions from both the quasar and the UVB. The optical depths in the proximity zone were then modified to produce the expected optical depths in the absence of the enhanced ionisation from the quasar. The preferred value of Γ_{bkg} was the one for which the resulting mean flux in the proximity zone was equal to that of the average Ly α forest at the same redshift.

We investigated a wide range of potential errors and biases affecting the proximity effect measurements using full radiative transfer simulations. We found the error in Γ_{bkg} for an individual line of sight to be dominated by the error in the quasar redshift

and τ_{eff} . The redshift errors for the sample are generally ≤ 0.01 , with several having a very accurate systemic redshift from CO and Mg II. An error in the assumed luminosity of the quasar of up to 40 per cent would still have a smaller effect than the typical redshift errors. Our raw measurements of the UVB intensity from individual sight lines at $z = 5$ should be typically overestimated by a factor of two, with random errors that are also roughly a factor of two. The largest biases result from the finite S/N of the spectra and the quasar lying in an overdensity (50 and 30 per cent, respectively). At $z = 6$, the UVB is overestimated by 30 per cent, with a factor of 2.5 random error. The largest source of bias at this redshift is the uncertainty in τ_{eff} .

Systematic uncertainties caused by the overdensity of matter close to the quasar were found to be smaller at $z > 5$ than at lower redshifts. The effect of the quasars lying in large-scale overdensities was found to be small for host halo masses of $M \leq 10^{12.2} M_{\odot}$, the most massive halos in our largest ($80h^{-1}$ comoving Mpc) simulation. Even in a toy model emulating the density distribution surrounding a $10^{13} M_{\odot}$ halo at $z = 6$, (and therefore as massive as the most massive haloes in the Millennium simulation at this redshift) large-scale overdensities were not dominating the error budget. This is due to the proximity regions (as defined in this paper) being substantially larger than the scale of the overdensities. It is however noted that at lower redshifts, where the UVB intensity and the mean flux level are higher, proximity regions may well be of similar size to the local overdensity. This effect is therefore likely very important at $z \sim 2 - 3$, where discrepancies between measurements from flux decrements and the proximity effect have been noted (Rollinde et al. 2005; Guimarães et al. 2007).

We also tested the effect of Lyman limit systems (LLS) Using the recent measurements of the frequency of LLS at high redshift from Songaila & Cowie (2010), we found that LLS have also only a small effect on our analysis, potentially causing us to overestimate Γ_{bkg} in our combined samples at $z \sim 5$ and 6 by roughly 0.1 dex.

Our measurements further assume that the gas temperature within the proximity region is similar to that in the general IGM. A thermal proximity effect, could have a sizeable impact on our estimates of the UVB intensity. If the gas in the ~ 5 proper Mpc of the proximity region closest to the quasar were e.g. on average 10^4 K hotter than the general IGM then the UVB will be *underestimated* by 0.14 (0.21) dex at $z = 5$ (6). This is comparable in magnitude to the biases from other environmental factors, although opposite in sign.

The results quoted in this paper are corrected for these biases, except the environmental biases due to a different gas temperature and average gas density, and the presence of LLS in the proximity zone. We have, however, demonstrated these biases are small or, in case of the temperature, are poorly observationally constrained.

Our measured values of Γ_{bkg} , corrected for biases, decline significantly from $z \sim 5$ to 6. For $z \sim 5$ we find $\log(\Gamma_{\text{bkg}}) = -12.15 \pm 0.16$ (0.32) at 68 (95) per cent confidence, whilst at $z \sim 6$ we find $\log(\Gamma_{\text{bkg}}) = -12.77 \pm 0.18$ (0.36), a decline significant at roughly the 3σ level. Within our sample, the UVB intensity measured from individual sight lines is seen to decline smoothly with redshift over $4.6 < z < 6.4$, but show no sign of the rapid decline which may be expected in the late stages of reionization when there is a rapid change in the attenuation length of ionising photons.

Our results are in good agreement with UVB estimates from measurements of the mean flux decrement in the redshift range $z = 5 - 6$, assuming an IGM temperature $T_0 = 10^4$ K. Both the proximity effect and flux decrement measurements imply a de-

cline in the intensity of the UVB by nearly an order of magnitude from $z = 4$ to $z = 6$.

Finally, we have combined our estimates of Γ_{bkg} with the evolution of the mean free path measured by Songaila & Cowie (2010). At face value the combined measurements imply a decline in the ionising emissivity of a factor of about 2 from $z \sim 5$ to 6, but it is important to keep in mind that at these redshifts measurements of the mean free path of ionising photons are extremely difficult, and that with such a low emissivity reionization could barely have been completed by $z = 6.4$.

The results presented here represent some of the highest redshift measurements of the UV background made to date, enabling us to probe deeper into the late(st) stages of hydrogen reionization. The next generation of optical and NIR telescopes will enable access to high signal-to-noise quasar spectra at even higher redshifts, leading to improved measurements of the ionising background and helping to establish a more complete picture of the final stages of the hydrogen reionization epoch.

ACKNOWLEDGMENTS

The authors would like to thank the anonymous referee for helpful comments, and Max Pettini and Richard McMahon for constructive and useful conversations during the course of this study. The authors are grateful to the staff at Keck and Magellan for making these observations possible. We also wish to recognise and acknowledge the very significant cultural role and reverence that the summit of Mauna Kea has always had within the indigenous Hawaiian community. We are most fortunate to have the opportunity to conduct observations from this mountain. The hydrodynamical simulations used in this work were performed in cooperation with SGI/Intel using the COSMOS facility hosted by the Department of Applied Mathematics and Theoretical Physics (DAMTP) at the University of Cambridge. COSMOS is a UK-CCC facility supported The Higher Education Funding Council for England (HEFCE) and the UK Science and Technology Facilities Council (STFC). We would like to thank STFC for financial support. GB acknowledges financial support from the Kavli foundation. JB has been supported by an ARC Australian postdoctoral fellowship (DP0984947).

REFERENCES

- Adelberger K. L., Steidel C. C., Shapley A. E., Pettini M., 2003, *ApJ*, 584, 45
- Bajtlik S., Duncan R. C., Ostriker J. P., 1988, *ApJ*, 327, 570
- Bechtold J., Weymann R. J., Lin Z., Malkan M. A., 1987, *ApJ*, 315, 180
- Becker G. D., Bolton J. S., Haehnelt M. G., Sargent W. L. W., 2010, *ArXiv e-prints*
- Becker G. D., Rauch M., Sargent W. L. W., 2007, *ApJ*, 662, 72
- Becker G. D., Sargent W. L. W., Rauch M., Simcoe R. A., 2006, *ApJ*, 640, 69
- Bornstein R., Sheckman S. A., Gunnels S. M., Mochnacki S., Athey A. E., 2003, in Presented at the Society of Photo-Optical Instrumentation Engineers (SPIE) Conference, Vol. 4841, M. Iye & A. F. M. Moorwood, ed, Society of Photo-Optical Instrumentation Engineers (SPIE) Conference Series, p. 1694
- Bolton J. S., Becker G. D., 2009, *MNRAS*, 398, L26

- Bolton J. S., Becker G. D., Wyithe J. S. B., Haehnelt M. G., Sargent W. L. W., 2010, *MNRAS*, 406, 612
- Bolton J. S., Haehnelt M. G., 2007a, *MNRAS*, 374, 493
- Bolton J. S., Haehnelt M. G., 2007b, *MNRAS*, 382, 325
- Bolton J. S., Haehnelt M. G., Viel M., Springel V., 2005, *MNRAS*, 357, 1178
- Bonoli S., Marulli F., Springel V., White S. D. M., Branchini E., Moscardini L., 2009, *MNRAS*, 396, 423
- Bouwens R. J., Illingworth G. D., Blakeslee J. P., Franx M., 2006, *ApJ*, 653, 53
- Bouwens R. J. et al., 2009, *ApJ*, 705, 936
- Bouwens R. J., Illingworth G. D., Franx M., Ford H., 2008, *ApJ*, 686, 230
- Bouwens R. J. et al., 2010, *ArXiv e-prints*
- Bunker A. J., Stanway E. R., Ellis R. S., McMahon R. G., 2004, *MNRAS*, 355, 374
- Carilli C. L. et al., 2010, *ApJ*, 714, 834
- Carswell R. F., Webb J. K., Baldwin J. A., Atwood B., 1987, *ApJ*, 319, 709
- Carswell R. F., Whelan J. A. J., Smith M. G., Boksenberg A., Tytler D., 1982, *MNRAS*, 198, 91
- Cooke A. J., Espey B., Carswell R. F., 1997, *MNRAS*, 284, 552
- Cristiani S., D'Odorico S., Fontana A., Giallongo E., Savaglio S., 1995, *MNRAS*, 273, 1016
- da Ângela J. et al., 2008, *MNRAS*, 383, 565
- Dall'Aglio A., Gnedin N. Y., 2010, *ApJ*, 722, 699
- Dall'Aglio A., Wisotzki L., Worseck G., 2008, *A&A*, 491, 465
- Dall'Aglio A., Wisotzki L., Worseck G., 2009, *ArXiv e-prints*
- D'Odorico V., Bruscoli M., Saitta F., Fontanot F., Viel M., Cristiani S., Monaco P., 2008, *MNRAS*, 389, 1727
- Eisenstein D. J., Hu W., 1999, *ApJ*, 511, 5
- Espey B. R., 1993, *ApJ*, 411, L59
- Fan X. et al., 2004, *AJ*, 128, 515
- Fan X. et al., 2001, *AJ*, 122, 2833
- Fan X. et al., 2006a, *AJ*, 132, 117
- Fan X. et al., 2006b, *AJ*, 131, 1203
- Fan X. et al., 2003, *AJ*, 125, 1649
- Fardal M. A., Giroux M. L., Shull J. M., 1998, *AJ*, 115, 2206
- Faucher-Giguère C., Lidz A., Zaldarriaga M., Hernquist L., 2008, *ApJ*, 673, 39
- Fontanot F., Monaco P., Cristiani S., Tozzi P., 2006, *MNRAS*, 373, 1173
- Furlanetto S. R., Mesinger A., 2009, *MNRAS*, 394, 1667
- Gnedin N. Y., Fan X., 2006, *ApJ*, 648, 1
- Granato G. L., De Zotti G., Silva L., Bressan A., Danese L., 2004, *ApJ*, 600, 580
- Guimarães R., Petitjean P., Rollinde E., de Carvalho R. R., Djorgovski S. G., Srianand R., Aghaee A., Castro S., 2007, *MNRAS*, 377, 657
- Haardt F., Madau P., 1996, *ApJ*, 461, 20
- Haardt F., Madau P., 2001, in D. M. Neumann & J. T. V. Tran, ed, *Clusters of Galaxies and the High Redshift Universe Observed in X-rays*
- Jena T. et al., 2005, *MNRAS*, 361, 70
- Kim Y., Croft R., 2007, *ArXiv Astrophysics e-prints*
- Kirkman D., Tytler D., 2008, *MNRAS*, 391, 1457
- Kirkman D. et al., 2005, *MNRAS*, 360, 1373
- Komatsu E. et al., 2009, *ApJS*, 180, 330
- Kulkarni V. P., Fall S. M., 1993, *ApJ*, 413, L63
- Lidz A., McQuinn M., Zaldarriaga M., Hernquist L., Dutta S., 2007, *ApJ*, 670, 39
- Liske J., Williger G. M., 2001, *MNRAS*, 328, 653
- Loeb A., Eisenstein D. J., 1995, *ApJ*, 448, 17
- Lu L., Sargent W. L. W., Womble D. S., Takada-Hidai M., 1996, *ApJ*, 472, 509
- Maselli A., Ferrara A., Gallerani S., 2009, *MNRAS*, 395, 1925
- McDonald P., Miralda-Escudé J., 2001, *ApJ*, 549, L11
- Meiksin A., White M., 2004, *MNRAS*, 350, 1107
- Mesinger A., Furlanetto S., 2009, *MNRAS*, 400, 1461
- Miralda-Escudé J., 2003, *ApJ*, 597, 66
- Miralda-Escudé J., Haehnelt M., Rees M. J., 2000, *ApJ*, 530, 1
- Murdoch H. S., Hunstead R. W., Pettini M., Blades J. C., 1986, *ApJ*, 309, 19
- Oesch P. A. et al., 2010, *ApJ*, 709, L16
- Ouchi M. et al., 2009, *ApJ*, 706, 1136
- Pascarella S. M., Lanzetta K. M., Chen H., Webb J. K., 2001, *ApJ*, 560, 101
- Pentericci L. et al., 2002, *AJ*, 123, 2151
- Péroux C., McMahon R. G., Storrie-Lombardi L. J., Irwin M. J., 2003, *MNRAS*, 346, 1103
- Prochaska J. X., O'Meara J. M., Worseck G., 2010, *ApJ*, 718, 392
- Rauch M. et al., 1997, *ApJ*, 489, 7
- Richard J., Pelló R., Schaerer D., Le Borgne J., Kneib J., 2006, *A&A*, 456, 861
- Richard J., Stark D. P., Ellis R. S., George M. R., Egami E., Kneib J., Smith G. P., 2008, *ApJ*, 685, 705
- Richards G. T., Vanden Berk D. E., Reichard T. A., Hall P. B., Schneider D. P., SubbaRao M., Thakar A. R., York D. G., 2002, *AJ*, 124, 1
- Rollinde E., Srianand R., Theuns T., Petitjean P., Chand H., 2005, *MNRAS*, 361, 1015
- Schirber M., Miralda-Escudé J., McDonald P., 2004, *ApJ*, 610, 105
- Scott J., Bechtold J., Dobrzycki A., Kulkarni V. P., 2000, *ApJS*, 130, 67
- Scott J. E., Kriss G. A., Brotherton M., Green R. F., Hutchings J., Shull J. M., Zheng W., 2004, *ApJ*, 615, 135
- Shapley A. E., Steidel C. C., Pettini M., Adelberger K. L., Erb D. K., 2006, *ApJ*, 651, 688
- Sijacki D., Springel V., Haehnelt M. G., 2009, *MNRAS*, 400, 100
- Songaila A., 2004, *AJ*, 127, 2598
- Songaila A., Cowie L. L., 2010, *ApJ*, 721, 1448
- Songaila A., Hu E. M., Cowie L. L., McMahon R. G., 1999, *ApJ*, 525, L5
- Springel V., 2005, *MNRAS*, 364, 1105
- Springel V. et al., 2005, *Nat*, 435, 629
- Srbínovsky J. A., Wyithe J. S. B., 2010, *Publications of the Astronomical Society of Australia*, 27, 110
- Stark D. P., Ellis R. S., Richard J., Kneib J., Smith G. P., Santos M. R., 2007, *ApJ*, 663, 10
- Steidel C. C., Adelberger K. L., Giavalisco M., Dickinson M., Pettini M., 1999, *ApJ*, 519, 1
- Storrie-Lombardi L. J., McMahon R. G., Irwin M. J., Hazard C., 1994, *ApJ*, 427, L13
- Telfer R. C., Zheng W., Kriss G. A., Davidsen A. F., 2002, *ApJ*, 565, 773
- Theuns T., Leonard A., Efstathiou G., Pearce F. R., Thomas P. A., 1998, *MNRAS*, 301, 478
- Tytler D., 1987, *ApJ*, 321, 69
- Tytler D. et al., 2004, *ApJ*, 617, 1
- Utsumi Y., Goto T., Kashikawa N., Miyazaki S., Komiyama Y., Furusawa H., Overzier R., 2010, *ApJ*, 721, 1680
- Vogt S. S. et al., 1994, in *Society of Photo-Optical Instrumentation Engineers (SPIE) Conference Series*, Vol. 2198, D. L. Crawford

- & E. R. Craine, ed, Society of Photo-Optical Instrumentation Engineers (SPIE) Conference Series, p. 362
- Williger G. M., Baldwin J. A., Carswell R. F., Cooke A. J., Hazard C., Irwin M. J., McMahon R. G., Storrie-Lombardi L. J., 1994, *ApJ*, 428, 574
- Wyithe J. S. B., Loeb A., 2004, *Nat*, 432, 194
- Wyithe S., Bolton J. S., 2010, ArXiv e-prints
- Yoshida M. et al., 2006, *ApJ*, 653, 988

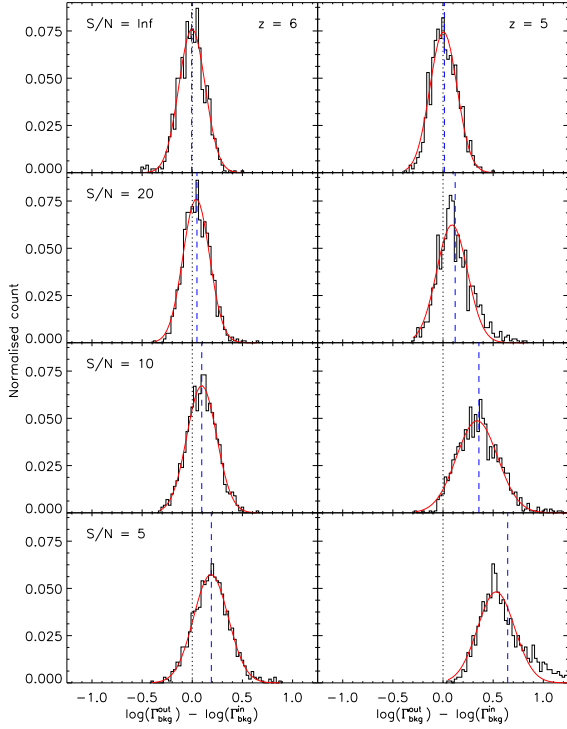


Figure A1. Distribution of the estimated values of $\log(\Gamma_{\text{bkg}})$ as a function of S/N for 1000 simulated spectra with HIRES resolution. A proximity region size of 10 Mpc is assumed. Apart from the luminosity of the quasar and the peculiar velocities of the gas, there are no other sources of error. The dotted line marks the input value, while the blue dashed line marks the mean of the simulated data set. The estimated values of $\log(\Gamma_{\text{bkg}})$ are well fit by a Gaussian.

APPENDIX A: DETAILED DISCUSSION OF THE ERROR ANALYSIS

In this Appendix we show how varying some of the parameters in Table 3 affects the scatter in $\log(\Gamma_{\text{bkg}})$ and induce a systematic bias. By modelling the effects of all these parameters, an expected sightline-to-sightline scatter, σ_{exp} , and bias, ϵ_{exp} , can be calculated for each individual quasar. The former contributes to our quoted errors in $\log(\Gamma_{\text{bkg}})$, and the latter is used such that $\log(\Gamma_{\text{bkg}}^{\text{corr}}) = \log(\Gamma_{\text{bkg}}^{\text{raw}}) - \epsilon_{exp}$. All values of $\log(\Gamma_{\text{bkg}})$ quoted in Table 5 have been corrected for these biases. For most of the spectra, the combined correction for all the sources of error is $\epsilon_{exp} \lesssim 0.2$ dex.

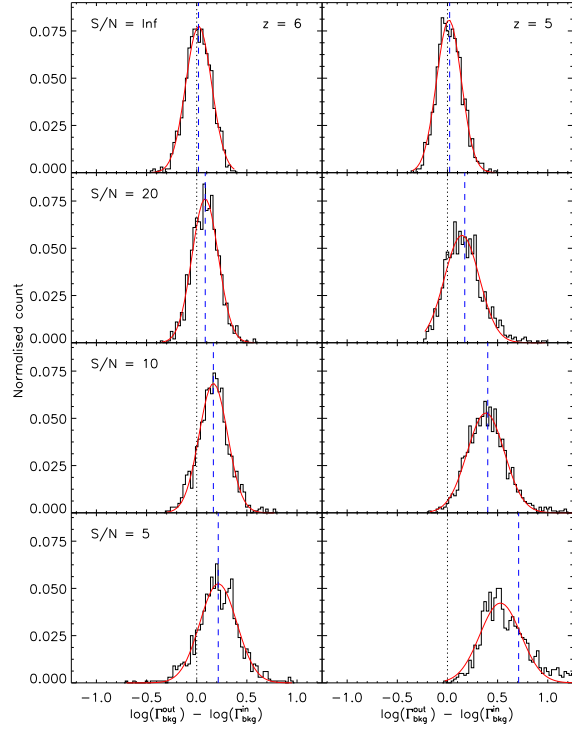


Figure A2. Same as Fig. A1 but for simulated data with MIKE velocity resolution.

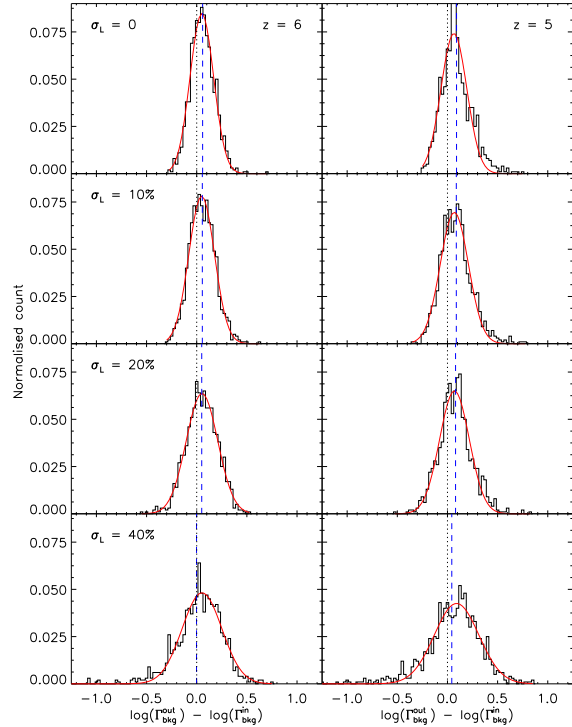


Figure A3. Expected distribution of errors in $\log(\Gamma_{\text{bkg}})$ for various errors in the luminosity, assuming a fixed S/N of 20, and HIRES resolution.

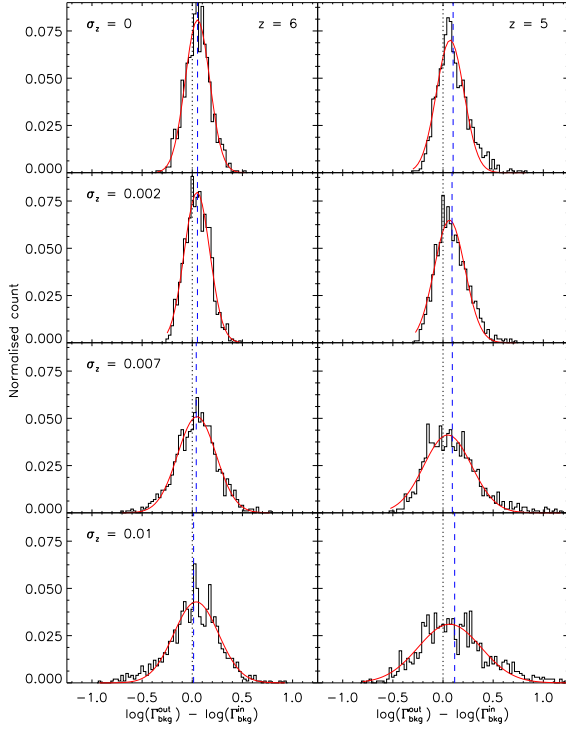


Figure A4. Expected distribution of errors in $\log(\Gamma_{\text{bkg}})$ for various errors in the redshift, for an assumed S/N of 20, and HIRES resolution. The top panels assume no redshift error. The next two panels down represent CO and Mg II redshifts, respectively, and the bottom panels represent the errors on redshifts determined from the onset of the Ly α forest.

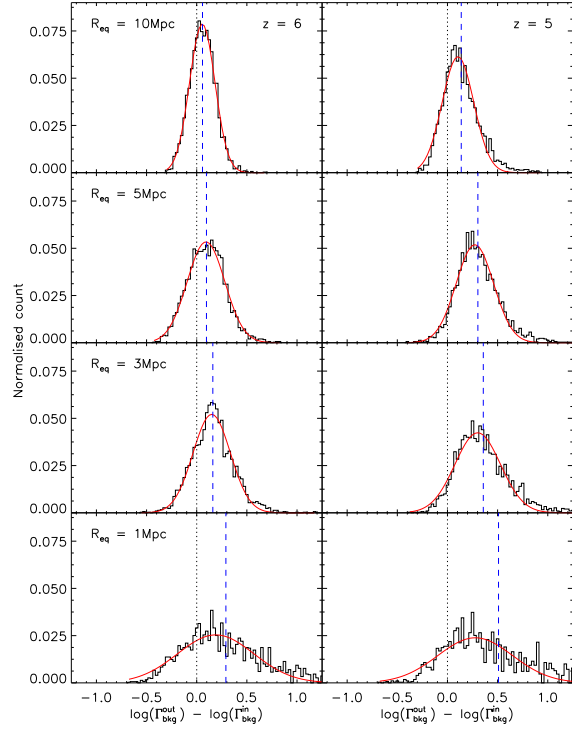


Figure A5. Expected distribution of errors in $\log(\Gamma_{\text{bkg}})$ for various input proximity region sizes (i.e. luminosity of the quasar), for a fixed S/N of 20, and HIRES resolution.

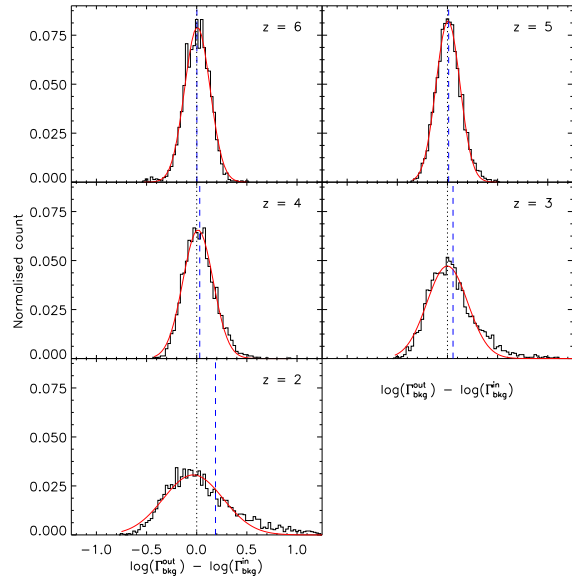


Figure A6. Expected distribution of errors in $\log(\Gamma_{\text{bkg}})$ for various quasar redshifts, for noiseless spectra (i.e. $S/N = \infty$), and at HIRES resolution. Even for noiseless data, the method struggles at lower redshift. The distribution loses its Gaussian symmetry, although the mode of the distribution does maintain its position close to the input value (see also Dall’Aglio et al. (2008)).